Cosmologically consistent analysis of gravitational waves from hidden sectors

Wan-Zhe Feng[1,*] Jinzheng Li[2,†] and Pran Nath[2,‡]

[1]*Center for Joint Quantum Studies and Department of Physics, School of Science, Tianjin University,*
Tianjin 300350, People's Republic of China
[2]*Department of Physics, Northeastern University, Boston, Massachusetts 02115-5000, USA*

Production of gravitational waves in the early Universe is discussed in a cosmologically consistent analysis within a first-order phase transition involving a hidden sector feebly coupled with the visible sector. Each sector resides in its own heat bath leading to a potential dependent on two temperatures and on two fields: one a standard model Higgs field and the other a scalar arising from a hidden sector $U(1)$ gauge theory. A synchronous evolution of the hidden and visible sector temperatures is carried out from the reheat temperature down to the electroweak scale. The hydrodynamics of two-field phase transitions, one for the visible and the other for the hidden is discussed, which leads to separate tunneling temperatures and different sound speeds for the two sectors. Gravitational waves emerging from the two sectors are computed and their imprint on the measured gravitational wave power spectrum vs frequency is analyzed in terms of bubble nucleation signature, i.e., detonation, deflagration, and hybrid. It is shown that the two-field model predicts gravitational waves accessible at several proposed gravitational wave detectors: LISA, DECIGO, BBO, and Taiji, and their discovery would probe specific regions of the hidden sector parameter space and may also shed light on the nature of bubble nucleation in the early Universe. The analysis presented here indicates that the cosmologically preferred models are those where the tunneling in the visible sector precedes the tunneling in the hidden sector and the sound speed c_s lies below its maximum, i.e., $c_s^2 < \frac{1}{3}$. It is of interest to investigate if these features are universal and applicable to a wider class of cosmologically consistent models.

I. INTRODUCTION

The observation of gravitational waves in black hole mergers in 2016 [1] opened up a new avenue to explore fundamental physics in a broader context using stochastic background of gravitational waves that arise from a variety of phenomena including those from cosmic phase transitions. The cosmic phase transitions occur at finite temperatures [2–6] and give rise to stochastic gravitational waves [7–9]. Several other sources of stochastic gravitational waves exist such as from the decay of the inflaton into standard model particles at the end of inflation [10–12]. It is also suggested that phase transitions may be linked to generation of matter-antimatter asymmetry, and especially

to baryogenesis [13–17]. The study of cosmic phase transitions involves finite temperature field theory which has been investigated in several early works [18,19]. A significant amount of further work already exists in this area, see, e.g., [20–43]. For reviews of phase transitions, see [44–46].

In the current analysis we discuss phase transitions and gravitational wave generation from hidden sectors that arise in supergravity, string, and extra-dimensional models, which improves on some of the previous works in that the analysis is cosmologically consistent. This implies a number of things that we mention briefly. First, the gravitational wave models need to satisfy constraints at different temperatures, e.g., at the tunneling temperature (10–100) GeV and at the big bang nucleosynthesis (BBN) temperature $\sim$1 MeV which requires an extrapolation over 4–5 orders of magnitude. This is due to the fact that at the tunneling temperature the phase transition is controlled in part by the parameter $\alpha = \epsilon/\rho$, where ϵ is the latent heat in the phase transition and ρ is the total energy density, which includes the energy density of the standard model and of the hidden sector. In general, the hidden sector and the visible sector are at different temperatures and we need to

*Contact author: vicf@tju.edu.cn
†Contact author: li.jinzh@northeastern.edu
‡Contact author: p.nath@northeastern.edu

know their precise correlation as a function of temperatures to compute α correctly. Further, as noted, we need to extrapolate to BBN time which constrains the extra degrees of freedom ΔN_{eff} above the standard model prediction, which requires we determine the hidden sector temperature at BBN time. Often this correlation is done by assuming separate entropy conservation in the visible sector and in the hidden sector. In this case, the ratio $\xi(T) = T_h/T$, where T_h is the temperature in the hidden sector and T is the temperature in the visible sector, is correlated with the ratio $\xi(T_0)$ at temperature T_0 so that

$$\frac{h_{\text{eff}}^h(\xi(T_0)T_0)}{h_{\text{eff}}^v(T_0)}\xi^3(T_0) = \frac{h_{\text{eff}}^h(\xi(T)T)}{h_{\text{eff}}^v(T)}\xi^3(T), \quad (1.1)$$

where h_{eff}^v and h_{eff}^h are the entropy degrees of freedom at their respective temperatures of the visible sector and of the hidden sector. However, it was shown in [47,48] that the separate entropy conservation approximation is highly inaccurate and leads to erroneous results for ΔN_{eff} by up to 500%. There is another basic problem with relations of the type above for cases where the decoupling in the dark sector occurs below the mass threshold of the dark particles. In this case the assumption of using thermal equilibrium to compute the effective degrees of freedom in the hidden sector breaks down as it gives essentially $h_{\text{eff}}^h(T_0) = 0$ requiring $\xi(T_0)$ to blow up. Here the accurate analysis used in this work is essential, as explained in Appendix E.

In the analysis we carry out a synchronous evolution of the temperatures in the visible and in the hidden sectors. Central to the analysis is the evolution equation for $\xi(T)$ which is solved together with the yield equations for the particles in the hidden sector and the visible sector with an assumed boundary condition on $\xi(T)$ at the reheat temperature, which leads to an accurate prediction for $\xi(T)$ at any temperature. There are also other aspects of the analysis that we briefly comment on. In the current analysis, we have nucleation arising from two bubble formations, one in the visible sector and the other in the hidden sector, and we give a combined treatment of both. This leads to two different critical temperatures and tunnelings arising from the visible sector and from the hidden sector. Further, often in gravitational wave analyses a sound speed of $c_s^2 = 1/3$ is assumed, which is the terminal relativistic speed of sound waves in a fluid. However, in the presence of true (broken) and false (symmetric) vacua for the visible and hidden sectors four different possibilities for the sound speed arise: with two possibilities for the visible sector depending on whether the vacuum is true or false and similarly for the hidden sector. We discuss these possibilities and show that the gravitational wave power spectrum depends sensitively on sound speed. Finally, we have investigated the possibility of identifying the nature of bubble dynamics and nucleation, i.e., detonation, deflagration, and hybrid for

their possible imprint on the gravitational wave spectrum. While we draw no firm conclusion, we notice that among the candidate models that satisfy all the constraints (i.e., constraints from first-order phase transition, from relic density, and from ΔN_{eff}), the hybrid nucleation modes exhibit the largest gravitational wave power spectrum.

The outline of the rest of the paper is as follows: In Sec. II we write the hidden sector model and discuss its temperature-dependent potential including thermal contributions to the field-dependent masses including the daisy summed multiloop contribution. Then we define the two-field potential including the temperature-dependent potential for the standard model Higgs field. In this section we also give a brief discussion of synchronous evolution of coupled hidden and visible sectors. In Sec. III we discuss nucleation and vacuum decay during phase transition for the case of a single field and then for the two-field case. In Sec. IV we discuss the hydrodynamics of bubble formation during phase transition. Here we discuss the sound velocity in the visible and in the hidden sectors for symmetric and broken phases and give an analysis of relativistic fluid equations and of bubble dynamics. Gravitational wave spectra arising from first-order phase transitions from the visible and the hidden sectors are discussed in Sec. V. A detailed numerical analysis of the gravitational wave power spectrum is given in Sec. VI. Thus, in Sec. VI A we exhibit the parameter space of models investigated in Monte Carlo simulations and the theoretical and experimental constraints placed on the allowed set of models. The nucleation temperature and the resulting gravity power spectrum are discussed in Sec. VI B. In Sec. VI C we discuss the effect of sound velocity on the gravitational wave power spectrum, and in Sec. VI D we investigate the dependence of sound velocity on the nucleation temperature. An analysis of the ΔN_{eff} constraint is given in Sec. VI D 1. In Sec. VI E we discuss the gravity power spectrum for different nucleation modes, i.e., detonation, deflagration, and hybrid. It is shown that a significant part of the parameter space of the assumed hidden sector model can be accessed by the planned space-based gravity experiments such as LISA, DECIGO, BBO, Taiji, and others. Conclusions are given in Sec. VII.

Additional details of the analysis are given in the Appendixes A–E. Thus, in Appendix A, we give further details of the temperature-dependent potential for the hidden sector and computation of temperature-dependent corrections to the bosonic masses for a $U(1)$ gauge theory including the contribution of the daisy resummation. In Appendix B, we give a summary of the known results on the temperature-dependent Higgs potential for the visible sector. In Appendix C, we give further details of visible and hidden sector interactions that enter in the combined analysis of the two sectors, and in Appendix D, we give the scattering cross sections that enter in the yield equations for the dark scalar, the dark fermion, and the dark gauge

boson. Finally, in Appendix E, we discuss the energy and pressure densities away from equilibrium as they are relevant for freeze-out and decoupling in the hidden sector.

II. TWO-FIELD PHASE TRANSITION INVOLVING THE STANDARD MODEL AND A HIDDEN SECTOR

As noted in the Introduction, cosmological phase transitions have been investigated in a significant number of previous works (for reviews, e.g., [45,49–51]). Most of the previous works using beyond the standard model (BSM) physics involve dynamics of only one field. Such an analysis does not fully take into account the effect of the standard model on computing the strength of the phase transition α in tunneling and the proper imposition of the ΔN_{eff} constraint at BBN time. Thus, as noted earlier a more complete analysis needs to consider an analysis involving BSM physics along with the standard model, which in our case implies a two-field analysis including the Higgs field of the standard model along with the Higgs field of the hidden sector. Further, since the visible sector and the hidden sector would normally be in different heat baths, the thermal potential governing the phase transition will depend on two temperatures, one of the visible and the other of the hidden sector. In the presence of a coupling between the two, as is most likely via a variety of portals, a synchronous evolution of the visible and the hidden sector temperature is essential for reliable predictions of phenomena related to the cosmological phase transition and specifically on predictions of the power spectrum of gravity waves resulting from the phase transition. This aspect of the cosmological phase transition is one of the focus points of the current analysis.

A. The hidden sector model and its temperature-dependent potential

We discuss now the case of phase transitions that involve two scalar fields, one of which is the standard models Higgs field and the other is a hidden sector Higgs scalar. In this case, we consider the Lagrangian of the form

$$\mathcal{L} = \mathcal{L}_{\mathrm{SM}} + \Delta\mathcal{L}, \tag{2.1}$$

where $\mathcal{L}_{\mathrm{SM}}$ is the standard model Lagrangian, and $\Delta\mathcal{L}$ is the hidden sector Lagrangian given by

$$\Delta\mathcal{L} = -\frac{1}{4}A_{\mu\nu}A^{\mu\nu} - |(\partial_\mu - ig_x A_\mu)\Phi|^2 - V_{\mathrm{eff}}^{\mathrm{h}}(\Phi)$$
$$- \bar{D}\left(\frac{1}{i}\gamma^\mu\partial_\mu + m_D\right)D - \frac{\delta}{2}A_{\mu\nu}B^{\mu\nu} - g_x Q_D \bar{D}\gamma^\mu D A_\mu, \tag{2.2}$$

where A_μ is the gauge field of the $U(1)_X$ of the hidden sector, D is the dark fermion, Φ is a complex scalar

field, and B_μ is the gauge field of the $U(1)_Y$, and $A_{\mu\nu} = \partial_\mu A_\nu - \partial_\nu A_\mu$ and $B_{\mu\nu} = \partial_\mu B_\nu - \partial_\nu B_\mu$. Thermal contributions to the zero temperature potential $V_{\mathrm{eff}}^{\mathrm{h}}(\Phi)$ will allow a first-order phase transition and a vacuum expectation value growth for the scalar field Φ generating a mass for the gauge boson A_μ and the scalar field in the hidden sector. Thus, the effective temperature-dependent hidden sector potential including loop corrections is given by

$$V_{\mathrm{eff}}^{\mathrm{h}}(\Phi, T_h) = V_{0h} + V_{1h}^{(0)} + \Delta V_{1h}^{(T_h)} + V_h^{\mathrm{daisy}}(T_h). \tag{2.3}$$

Here V_{0h} is the zero temperature tree potential, $V_{1h}^{(0)}$ is the one-loop Coleman-Weinberg zero temperature contribution, $\Delta V_{1h}^{(T_h)}$ is the one-loop thermal contribution, $V_{1h}^{\mathrm{daisy}}(T_h)$ is the daisy contribution from multiloop summation, and divergences are canceled off by counterterms. Thus, we have

$$V_{0h} = -\mu_h^2 \Phi\Phi^* + \lambda_h(\Phi^*\Phi)^2, \qquad \Phi = \frac{1}{\sqrt{2}}(\chi_c + \chi + iG_h^0), \tag{2.4}$$

where χ_c is the background field that enters in the tree level potential. Further, $V_{1h}^{(0)}(\chi)$, the one-loop effective potential at $T = 0$, is given by

$$V_{1h}^{(0)}(\chi_c) = \sum_i \frac{N_i(-1)^{2s_i}}{64\pi^2} m_i^4(\chi_c)\left[\ln\left(\frac{m_i^2(\chi_c)}{\Lambda_h^2}\right) - \mathcal{C}_i\right], \tag{2.5}$$

where N_i is the degrees of particle i and where the field-dependent masses of the hidden sector fields A_μ, χ, G_h^0 that enter the potential are given by

$$m_A^2(\chi_c) = g_x^2\chi_c^2, \qquad m^2(\chi_c) = -\mu_h^2 + 3\lambda_h\chi_c^2,$$
$$m_{G_h^0}^2(\chi_c) = -\mu_h^2 + \lambda_h\chi_c^2. \tag{2.6}$$

For the one-loop thermal correction, we have

$$\Delta V_{1h}^{(T_h)}(\chi_c, T_h) = \frac{T_h^4}{2\pi^2}\left[3J_B\left(\frac{m_A}{T_h}\right) + J_B\left(\frac{m_\chi}{T_h}\right) + J_B\left(\frac{m_{G_h^0}}{T_h}\right)\right], \tag{2.7}$$

where J_i $(i = B, F)$ is defined so that at one loop

$$J_i\left(\frac{m_i}{T_h}\right) = \int_0^\infty \mathrm{d}q\, q^2 \ln\left[1 \mp \exp\left(-\sqrt{q^2 + m_i^2/T_h^2}\right)\right],$$
$$i = (B, F), \tag{2.8}$$

where (B, F) stand for bosonic and fermionic cases. The daisy loop contributions are only for the longitudinal mode of A and χ and are given for mode $i = A, \chi$ so that

$$V^{\text{daisy}}(i, T_h) = -\frac{T_h}{12\pi} \{[m_i^2 + \Pi_i(T_h)]^{3/2} - m_i^3\}, \quad (2.9)$$

where $\Pi_i(T_h)$ is thermal contribution to the zero temperature mass m_i^2. For the longitudinal mode of A and for χ they are given by

$$\Pi_A(T_h) = \frac{2}{3}g_x^2 T_h^2, \quad \Pi_\chi(T_h) = \frac{1}{4}g_x^2 T_h^2 + \frac{1}{3}\lambda_h T_h^2. \quad (2.10)$$

A deduction of Eqs. (2.9) and (2.10) is given in Appendix A. We note that the daisy resummation correction to the effective potential is equivalent to replacing the particle mass in J_B function so that

$$m_i^2 \to [m_i^{(T_h)}]^2 \equiv m_i^2 + \Pi_i(T_h), \quad (2.11)$$

where $\Pi_i(T_h)$ is the self-energy of the bosonic field for particle i at finite temperature T_h, known as "Debye mass." Making the replacement of Eq. (2.11), the effective potential of Eq. (2.3) now takes the form

$$
\begin{aligned}
V_{\text{eff}}^h(\chi_c, T_h) &= V_{0h} + V_{1h}^{(0)}(\chi_c) + V_1^T(\chi_c, T_h) \\
&= \frac{\mu_h^2}{2}\chi_h^2 + \frac{\lambda_h}{4}\chi_h^4 + \sum_i \frac{g_i(-1)^{2s_i}}{64\pi^2}m_i^4(\chi_c)\left[\ln\left(\frac{m_i^2(\chi_c)}{\Lambda_h^2}\right) - \mathcal{C}_i\right] \\
&\quad + \frac{T_h^4}{2\pi^2}\sum_B g_B \int_0^\infty dq\, q^2 \ln\left[1 - \exp\left(-\sqrt{q^2 + \left[m_B^{(T_h)}\right]^2/T_h^2}\right)\right] \\
&\quad - \frac{T_h^4}{2\pi^2}\sum_F g_F \int_0^\infty dq\, q^2 \ln\left[1 + \exp\left(-\sqrt{q^2 + \left[m_F^{(T_h)}\right]^2/T_h^2}\right)\right].
\end{aligned}
\quad (2.12)
$$

This is the potential that is used in the analysis here. In this work we analyze a whole range of temperatures that encompass the regions $T_h \ll m$, $T_h \gg m$ and the regions in between. For this reason we do not use high T_h and low T_h expansions but rather use the full integral forms for J_B (and also for J_F in the standard model case). Further details on the thermal masses for the hidden sector are given in Appendix A and a summary of the temperature-dependent potential for the standard model including corrections due to thermal masses and daisy contributions is given in Appendix B.

Let us now consider the case of two sectors together but with no interactions between the scalar fields so that the scalar potential is simply a sum of potentials in the two sectors, i.e.,

$$V_{\text{eff}}(\phi_c, T; \chi_c, T_h) = V_{\text{eff}}^v(\phi_c, T) + V_{\text{eff}}^h(\chi_c, T_h). \quad (2.13)$$

where $V_{\text{eff}}^v(\phi_c, T)$ is the effective temperature-dependent Higgs potential in the standard model, which is well known, but for easy reference it is given in Appendix B. Here the minimization conditions are

$$V_{\text{eff},\phi_c}^v = 0, V_{\text{eff},\chi_c}^h = 0, V_{\text{eff},\phi_c\phi_c}^v > 0, V_{\text{eff},\chi_c\chi_c}^h > 0, \quad (2.14)$$

which imply that if the minimization conditions are individually satisfied in each sector then the minimization of the potential overall is also satisfied for the combined system of the visible and the hidden sectors. At the minimum of the potential we define $v = \phi_c$ and $v_h = \chi_c$. We note, however, that the two potentials are at different temperatures, one at T and the other at T_h, and for a synchronous minimization to occur in the two sectors T and T_h must be related by

$$T_h = \xi(T)T, \quad (2.15)$$

where $\xi(T)$ is determined by a synchronous evolution of the visible sector and the hidden sector from the reheating scale to the low temperature scale, where phase transitions occur with given initial condition on ξ_0 at the reheat temperature. In the absence of a synchronous evolution, ξ has been used [52] as a free parameter. However, such a procedure does not allow one to use temperature constraints consistently at different temperatures such as at the time of tunnelings, which occur at different temperatures for the visible and the hidden sector and to correlate them with the ΔN_{eff} constraint the BBN time. In this work, we will solve $\xi(T)$ as a function of T which gives more reliable results. Further, as noted earlier we can reliably extrapolate the data to BBN time to include the constraint from ΔN_{eff} [47,48,53] and from the relic density of dark matter.

B. Synchronous evolution of coupled hidden and visible sectors

We discuss below an analysis for the evolution of $\xi(T)$ which, in general, allows for any type of thermal contact

between the visible and the hidden sectors. Since the standard model explains quite accurately a large amount of data at the electroweak scale, the couplings between the hidden and the visible sectors need to be extra weak [54] or feeble. Such couplings could arise via a Higgs portal [55], kinetic mixing [56], or Stueckelberg mass mixing [57], or both [58], as well as other possible combinations such as a Stueckelberg-Higgs portal [59] or some higher-dimensional operator connecting the two sectors. Synchronous thermal evolution between the visible and one hidden sector was discussed in [60], the case with two hidden sectors was discussed in [61], and for multiple hidden sectors in [62]. Here we give a brief review of synchronous evolution central to the analysis of this work.

Thus, the energy densities for the visible and the hidden sectors obey the following coupled Boltzmann equations in an expanding universe:

$$\frac{d\rho_v}{dt} + 3H(\rho_v + p_v) = j_v,$$
$$\frac{d\rho_h}{dt} + 3H(\rho_h + p_h) = j_h. \quad (2.16)$$

Here ρ_v and p_v are the energy and momentum densities for the visible sector, and where (j_v, j_h) encode in them all the possible processes exchanging energy between these sectors. They are defined in Appendixes C and D. The total energy density $\rho = \rho_v + \rho_h$ satisfies the equation

$$\frac{d\rho}{dt} + 3H(\rho + p) = 0, \quad (2.17)$$

where $p = p_v + p_h$ is the total pressure density. We introduce the functions $\sigma_i = \frac{3}{4}(1 + \frac{p_i}{\rho_i})$, where $\sigma_1 = \sigma_v, \sigma_2 = \sigma_h$, where $\sigma_i = \frac{3}{4}$ for matter dominance, and $\sigma_i = 1$ for radiation dominance. Similarly, we define $\sigma = \frac{3}{4}(1 + \frac{p}{\rho})$. We note that σ_v, σ_h, and σ are temperature dependent and this

dependence is taken into account in the evolution equations. Using σ_i and σ, the ρ_i and ρ evolution equations read

$$\frac{d\rho_i}{dt} + 4H\sigma_i\rho_i = j_i, (i = v, h), \quad \frac{d\rho}{dt} + 4H\sigma\rho = 0. \quad (2.18)$$

We will use temperature instead of time and temperature of the visible sector T as the clock. In this case we can write the evolution equations in terms of T using the relation

$$\frac{dT}{dt} = -4H\sigma\rho\left(\frac{d\rho}{dT}\right)^{-1}, \quad (2.19)$$

and $d\rho_i/dt = (d\rho_i/dT)(dT/dt)$. Further, we can deduce the following evolution equation for $\xi(T)$ which governs the temperature evolution of the hidden sector relative to that of the visible sector

$$\frac{d\xi}{dT} = \left[-\xi\frac{d\rho_h}{dT_h} + \frac{4H\sigma_h\rho_h - j_h}{4H\sigma\rho - 4H\sigma_h\rho_h + j_h}\frac{d\rho_v}{dT}\right]\left(T\frac{d\rho_h}{dT_h}\right)^{-1}, \quad (2.20)$$

where j_h is defined in Eq. (D6). The above analysis is general, allowing for any type of thermal contact via any type of portal. In the analysis here we assume a kinetic mixing and do not consider Stueckelberg mass mixing as it would lead to millicharges for dark matter [57,63–65]. Thus, we include in the Lagrangian a term $-\frac{\delta}{2}A^{\mu\nu}B_{\mu\nu}$ where $B_{\mu\nu}$ is the field strength of $U(1)_Y$ hypercharge field B_μ. Further details of the interactions between the visible and the hidden sector in the canonically diagonalized basis are given in Appendix C.

The evolution equation for $\xi(T)$, Eq. (2.20) involves j_h which depends on the yields of the hidden sector $Y_D, Y_{\gamma'}$, and Y_χ (see Appendix D). We discuss the Boltzmann equations for the yields below

$$\frac{dY_D}{dT} = -\frac{\mathbb{s}}{H}\left(\frac{d\rho_v/dT}{4\sigma\rho - 4\sigma_h\rho_h + j_h/H}\right)\left[\frac{1}{2}\langle\sigma v\rangle_{D\bar{D}\to i\bar{i}}(T)(Y_D^{eq}(T)^2 - Y_D^2) - \frac{1}{2}\langle\sigma v\rangle_{D\bar{D}\to\gamma'\gamma'}(T_h)\left(Y_D^2 - Y_D^{eq}(T_h)^2\frac{Y_{\gamma'}^2}{Y_{\gamma'}^{eq}(T_h)^2}\right)\right], \quad (2.21)$$

$$\begin{aligned}\frac{dY_{\gamma'}}{dT} = -\frac{\mathbb{s}}{H}\left(\frac{d\rho_v/dT}{4\sigma\rho - 4\sigma_h\rho_h + j_h/H}\right)&\left[\frac{1}{2}\langle\sigma v\rangle_{D\bar{D}\to\gamma'\gamma'}(T_h)\left(Y_D^2 - Y_D^{eq}(T_h)^2\frac{Y_{\gamma'}^2}{Y_{\gamma'}^{eq}(T_h)^2}\right)\right.\\ &+ \frac{1}{2}\langle\sigma v\rangle_{\chi\bar{\chi}\to\gamma'\gamma'}(T_h)\left(Y_\chi^2 - Y_\chi^{eq}(T_h)^2\frac{Y_{\gamma'}^2}{Y_{\gamma'}^{eq}(T_h)^2}\right) + \langle\sigma v\rangle_{i\bar{i}\to\gamma'}(T)Y_i^{eq}(T)^2\\ &\left.- \frac{1}{\mathbb{s}}\langle\Gamma_{\gamma'\to i\bar{i}}(T_h)\rangle Y_{\gamma'} + \langle\Gamma_{\chi\to\gamma'\gamma'}(T_h)\rangle\left(Y_\chi - Y_\chi^{eq}(T_h)\frac{Y_{\gamma'}^2}{Y_{\gamma'}^{eq}(T_h)^2}\right)\right], \quad (2.22)\end{aligned}$$

$$\frac{dY_\chi}{dT} = -\frac{\mathbb{s}}{H}\left(\frac{d\rho_v/dT}{4\sigma\rho - 4\sigma_h\rho_h + j_h/H}\right)\left[-\frac{1}{2}\langle\sigma v\rangle_{\chi\bar{\chi}\to\gamma'\gamma'}(T_h)\left(Y_\chi^2 - Y_\chi^{\rm eq}(T_h)^2\frac{Y_{\gamma'}^2}{Y_{\gamma'}^{\rm eq}(T_h)^2}\right)\right.$$
$$\left. -\frac{1}{\mathbb{s}}\langle\Gamma_{\chi\to\gamma'\gamma'}(T_h)\rangle\left(Y_\chi - Y_\chi^{\rm eq}(T_h)\frac{Y_{\gamma'}^2}{Y_{\gamma'}^{\rm eq}(T_h)^2}\right)\right], \tag{2.23}$$

where $\mathbb{s}$ is the entropy density and yield for particle i is defined by $Y_i = n_i/\mathbb{s}$. In the analysis here we take account of the hidden sector energy density and pressure density, ρ_h and p_h, not only through thermal equilibrium analysis but also by accounting for the contribution of relic abundance. A further discussion of it is provided in Appendix E. For the computation of the visible sector density and pressure we use the precalculated values of $g_{\rm eff}^v$ and $h_{\rm eff}^v$ which are tabulated results from microOMEGAs [66]. We discuss next the bubble nucleation for the case of the single field first and then for the case of two fields.

III. NUCLEATION AND VACUUM DECAY

A. Single-field nucleation

Before proceeding to a discussion of nucleation for the two-field case, we first summarize the first-order phase transition involving the decay of the false vacuum into the true vacuum involving bubble nucleation of a generic scalar field ϕ. We define the temperature when bubbles start to nucleate as T_n. Here at zero temperature the decay probability per unit time and per unit volume is given by $\Gamma = Ke^{-S_4}$, where S_4 is the Euclidean action in four dimensions and K is typically of the fourth-order power of the energy involved in the phase transition [20]. At finite temperature the decay probability per unit time and per unit volume takes the form $\Gamma = K(T)e^{-S_3/T}$ where T is the temperature, and $K(T) \sim T^4$. Thus, for the case of a single scalar field, $S_3(T)$ is given by

$$S_3(T) = \int_0^\infty 4\pi r^2 dr\left[\frac{1}{2}\left(\frac{d\phi}{dr}\right)^2 + V_{\rm eff}^v(\phi, T)\right], \tag{3.1}$$

with the scalar field satisfying the Euclidean O(3) symmetry equation of motion and the appropriate boundary conditions

$$\frac{d^2\phi}{dr^2} + \frac{2}{r}\frac{d\phi}{dr} = \frac{\partial}{\partial\phi}V_{\rm eff}^v(\phi, T), \qquad \lim_{r\to\infty}\phi = 0,$$
$$\left.\frac{d\phi}{dr}\right|_{r=0} = 0. \tag{3.2}$$

We use the *Mathematica* package FindBounce [67,68] to numerically compute S_3. Once $S_3(T)$ is determined, the nucleation temperature T_n is defined so that

$$\int_0^{T_n}\frac{\Gamma dt}{H^3} = \int_{T_n}^\infty\frac{dT}{T}\left(\frac{90}{8\pi^3 g_{\rm eff}}\right)^2\left(\frac{M_{\rm Pl}}{T}\right)^4 e^{-S_3(T)/T} \simeq 1. \tag{3.3}$$

This equation is well approximated by $\frac{S_3(T_n)}{T_n} \sim 140$. Then the whole vacuum decay process can be characterized by the following temperatures: (1) critical temperature T_c, when the effective potential has two degenerate minima; (2) nucleation temperature T_n, when the transition occurs or when one bubble is nucleated in one casual Hubble volume; and (3) destabilization temperature T_0, when the original vacuum is no longer a minimum or when the potential barriers between the false vacuum and true vacuum disappears.

B. Two-field nucleation

For the two-field nucleation, the calculation here will become complicated because the over-undershoot implementation by some numerical analysis (like CosmoTransitions) is not reliable anymore. The work of [69] discusses such a problem in detail. Thus, here we provided a way that can deal with such a situation with the potential given by Eq. (2.13). For the visible (hidden) sector, there will be corresponding temperatures T_c, T_n, T_0 $(T_{h,c}, T_{h,n}, T_{h,0})$ with the following orders:

$$T_0 < T_n < T_c \qquad (T_{h,0} < T_{h,n} < T_{h,c}). \tag{3.4}$$

Since we have $\xi(T)$ to give us the temperature ratio of two sectors at each moment, if we know the temperature of the visible sector, we can then easily find the temperature in the hidden sector, with Eq. (2.15). Correspondingly, we define another function

$$T = \zeta(T_h)T_h, \tag{3.5}$$

which allows us to fix the temperature in the visible sector given the temperature in the hidden sector. We note that Eqs. (2.15) and (3.5) are equivalent so that $\zeta(T_h) = \xi(T)^{-1}$. It is convenient to use Eq. (2.15) [Eq. (3.5)] when the visible (hidden) sector temperature T (T_h) is used as the clock. Next we discuss different cases for the nucleation process.

Case 1: For this case, we have one of the scalar field's nucleation occurring first and then the other scalar field nucleation occurring separately at different time, which means the first scalar field already reaches its destabilization temperature before the other scalar field reaches

its critical temperature, i.e., $(T_0, T_c) \cap (\zeta(T_{h,0})T_{h,0}, \zeta(T_{h,c})T_{h,c}) = \emptyset$. For this case, the original vacuum decays first to an intermediate vacuum and then decays into the true vacuum. In this case, we can treat the two-field nucleation as two single-field vacuum decay problems. Here T_n and $T_{h,n}$ can be determined by Eqs. (3.1)–(3.3).

Case 2: For the second case, we have the visible scalar field nucleation and the hidden scalar field nucleation going through the vacuum decay at the same time, which means one of the scalar fields reaches its critical temperature before the other scalar field reaches its destabilization temperature, i.e., $(T_0, T_c) \cap (\zeta(T_{h,0})T_{h,0}, \zeta(T_{h,c})T_{h,c}) \neq \emptyset$. For this case, it is possible that the original vacuum decays directly to the final true vacuum and we will have only one transition. Here let us first assume that $T_c < \zeta(T_{h,c})T_{h,c}$, so we have

$$T_0 < \zeta(T_{h,0})T_{h,0} < T_c < \zeta(T_{h,c})T_{h,c}. \qquad (3.6)$$

Figure 1 shows a schematic diagram for such a case. If the first nucleation occurs at $T_c < T < \zeta(T_{h,c})T_{h,c}$, then it will be the same as in case 1 where there will be an intermediate

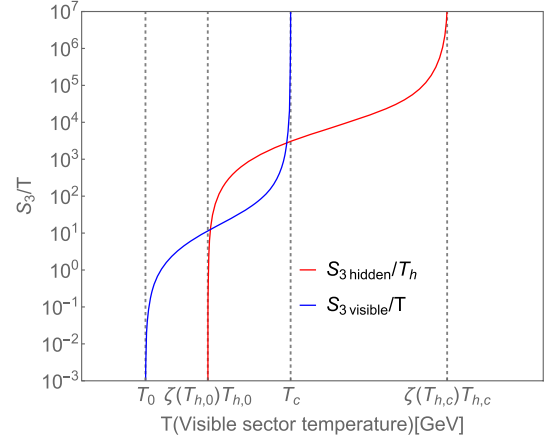

FIG. 1. Schematic plot for Case 2. $S_3(T)/T$ vs T for S_{3v} and S_{3h}.

vacuum. If not, then we need consider the possibility that the original vacuum decays directly to the final true vacuum. According to Eq. (2.13), there is no interaction between two scalar fields in the potential, i.e., there is no term like $\phi\chi$. In this case $S_{3\text{total}}(T)$ is given by

$$
\begin{aligned}
S_{3\text{total}}(T) &= \int_0^\infty 4\pi r^2 dr \left[\frac{1}{2}\left(\frac{d\phi}{dr}\right)^2 + \frac{1}{2}\left(\frac{d\chi}{dr}\right)^2 + V_{\text{eff}}(\phi, T; \chi, \xi(T)T)\right] \\
&= \int_0^\infty 4\pi r^2 dr \left[\frac{1}{2}\left(\frac{d\phi}{dr}\right)^2 + V_{\text{eff}}^v(\phi, T)\right] + \int_0^\infty 4\pi r^2 dr \left[\frac{1}{2}\left(\frac{d\chi}{dr}\right)^2 + V_{\text{eff}}^h(\chi, \xi(T)T)\right] \\
&= S_{3v}(T) + S_{3h}(\xi(T)T).
\end{aligned} \qquad (3.7)
$$

Here the equations of motion are to be solved with Euclidean $O(3)$ symmetry and with appropriate boundary conditions so that

$$\frac{d^2\phi}{dr^2} + \frac{2}{r}\frac{d\phi}{dr} = \frac{\partial}{\partial\phi}V_{\text{eff}}(\phi, T; \chi, \xi(T)T) = \frac{\partial}{\partial\phi}V_{\text{eff}}^v(\phi, T), \qquad \lim_{r\to\infty}\phi = 0, \qquad \left.\frac{d\phi}{dr}\right|_{r=0} = 0. \qquad (3.8)$$

$$\frac{d^2\chi}{dr^2} + \frac{2}{r}\frac{d\chi}{dr} = \frac{\partial}{\partial\chi}V_{\text{eff}}(\phi, T; \chi, \xi(T)T) = \frac{\partial}{\partial\chi}V_{\text{eff}}^h(\chi, T_h), \qquad \lim_{r\to\infty}\chi = 0, \qquad \left.\frac{d\chi}{dr}\right|_{r=0} = 0. \qquad (3.9)$$

Since the above two equations can be solved independently, we can just treat each as a single-field case. To find T_n for the case where the original vacuum decays directly to the final true vacuum, we first assume that such a nucleation happens at $T_{n,\text{total}}$ and get

$$\frac{S_{3\text{total}}(T_{n,\text{total}})}{T_{n,\text{total}}} = \frac{S_{3v}(T_{n,\text{total}})}{T_{n,\text{total}}} + \frac{S_{3h}(\xi(T_{n,\text{total}})T_{n,\text{total}})}{T_{n,\text{total}}} \sim 140, \qquad (3.10)$$

which tells us that $\frac{S_{3v}(T_{n,\text{total}})}{T_{n,\text{total}}} < 140$. However, S_{3v}/T is a monotonic increasing function of T which leads to

$$\exists T_n > T_{n,\text{total}}: \quad \frac{S_{3v}(T_n)}{T_n} \sim 140. \qquad (3.11)$$

It tells us that, before the original vacuum decays directly into the final true vacuum, it must decay into an intermediate vacuum first. However, it takes some time for the phase transition to complete after the temperature reaches
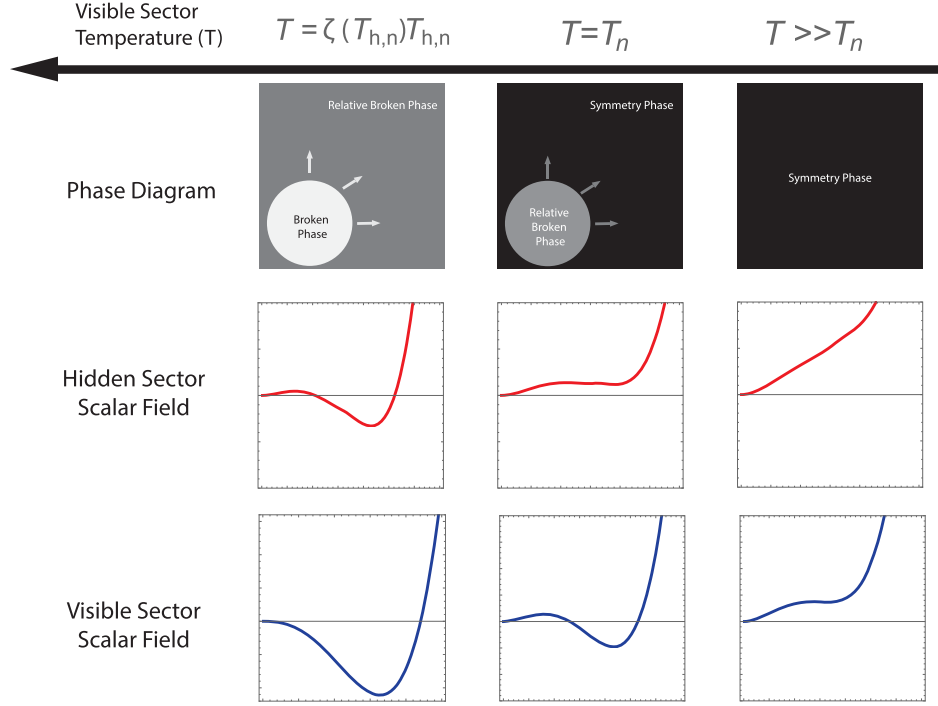
FIG. 2.   A schematic diagram for the two-step phase transition. The phase of the whole Universe transfers from the symmetry phase to the relative broken phase before ultimately reaching the fully broken phase. The plots of $V_{\text{eff}}^{\text{v}}$ vs ϕ and $V_{\text{eff}}^{\text{h}}$ vs χ are shown for different temperatures.

the nucleation temperature. Thus, it is possible that the other sector also reaches its nucleation temperature during this process. It will become more complicated but interesting because now the gravitational wave will be generated by the collision of two types of bubbles from two different sectors. We note, however, that the interaction between the sectors is too feeble to produce any effect. Further, we assume the phase transition is completed immediately after it reaches the nucleation temperature to avoid this problem altogether. Therefore, case 2 can be treated the same as case 1 and we have shown that, in any case, we can treat the problem as two single-field vacuum decay problems. The whole transition will undergo through two-step phase transition at two different nucleation temperatures T_n and $T_{h,n}$. For each phase transition, there will be a "relative symmetry phase" and a "relative broken phase." A schematic diagram of the entire nucleation process is given by Fig. 2.

IV. HYDRODYNAMICS OF BUBBLE FORMATION DURING PHASE TRANSITION

To investigate the gravitational wave generation from cosmological phase transition, we need to first study the hydrodynamics of bubble formation during the phase transition. One of the important elements in the hydrodynamics of bubbles is the sound velocity in the fluid in the symmetric phase and in the broken phase and it is model dependent. We discuss this next.

A. Sound velocities in the visible and in the hidden sectors

Sound velocity in fluids is known to have a terminal value so that $c_s^2 = 1/3$. However, its actual value depends on whether the phase is unbroken or broken and on the type of the broken phase. We start with the thermodynamic quantities: energy density e, pressure p, and enthalpy density w. They are, in general, given by the following equations:

$$p = -\mathcal{F}, \qquad e = T\frac{\partial p}{\partial T} - p, \qquad w = p + e. \quad (4.1)$$

Here $\mathcal{F}$ is the free energy density where p is given by

$$p(\phi, T; \chi, T_h) = p_v(\phi, T) + p_h(\chi, T_h), \quad (4.2)$$

$$p_v(\phi, T) = \frac{\pi^2}{90}g_{\text{eff}}^v T^4 - V_{\text{eff}}^{\text{v}}(\phi, T), \quad (4.3)$$

$$p_h(\chi, T_h) = \frac{\pi^2}{90}g_{\text{eff}}^h T_h^4 - V_{\text{eff}}^{\text{h}}(\chi, T_h). \quad (4.4)$$

Correspondingly, we have

$$e(\phi, T; \chi, T_h) = e_v(\phi, T) + e_h(\chi, T_h) + e_{\text{mix}}(\phi, T, \chi, T_h), \quad (4.5)$$

$$e_v(\phi, T) = T\frac{\partial p_v}{\partial T} - p_v, \quad e_h(\chi, T_h) = T_h\frac{\partial p_h}{\partial T_h} - p_h, \qquad (4.6)$$

$$e_{\mathrm{mix}}(\phi, T; \chi, T_h) = T^2 \frac{\partial p_h}{\partial T_h}\frac{\partial \xi}{\partial T}, \qquad (4.7)$$

and for the sound velocity $c_s^2 = dp/de$ (total derivative here), we have

$$c_s^2(\phi, \chi; T, T_h) = \frac{\frac{\partial(p_v)}{\partial T} + \frac{\partial(p_h)}{\partial T_h}\frac{\partial(T_h)}{\partial T}}{\frac{\partial(e_v)}{\partial T} + \frac{\partial(e_h)}{\partial T_h}\frac{\partial(T_h)}{\partial T} + \frac{\partial e_{\mathrm{mix}}}{\partial T}}, \qquad (4.8)$$

where

$$\frac{\partial T_h}{\partial T} = \frac{\partial(\xi T)}{\partial T} = \frac{\partial \xi}{\partial T}T + \xi(T), \qquad (4.9)$$

and where we used $\frac{dp_v}{dT} = \frac{\partial p_v}{\partial T}, \frac{de_v}{dT} = \frac{\partial e_v}{\partial T}$ since we are interested in sound velocity in vacuums. Further, since explicit integrals for p_h, e_h are known, and numerical tables for the corresponding visible sector quantities are known, an evaluation of $\partial(p_v)/\partial T, \partial(e_v)/\partial T$ and $\partial(p_h)/\partial T_h, \partial(e_h)/\partial T_h$ can be numerically carried out. According to the analysis in Sec. III, there will actually be two sets of symmetry phase velocities and broken phase velocities possible. For the visible scalar field nucleation, the sound velocity in the symmetric phase and in the broken phase, i.e., sound velocity outside and inside the bubble of the visible scalar field nucleation, will be labeled $c_{s,+,v}$ and $c_{s,-,v}$. Similarly, for the hidden scalar field nucleation, we have $c_{s,+,h}$ and $c_{s,-,h}$.

We label vacua in the broken phase case for the visible and hidden sectors to be ϕ_{min} and χ_{min}, and they are found numerically. For the case when nucleation in the visible sector occurs before nucleation in the hidden sector, i.e., $T_n > \zeta(T_{h,n})T_{h,n}$, these four velocities are given by

$$\begin{aligned}
c_{s,+,v}^2 &= c_s^2(0, 0, T_n, \xi(T_n)T_n),\\
c_{s,-,v}^2 &= c_s^2(\phi_{\mathrm{min}}, 0, T_n, \xi(T_n)T_n),\\
c_{s,+,h}^2 &= c_s^2(\phi_{\mathrm{min}}, 0, \zeta(T_{h,n})T_{h,n}, T_{h,n}),\\
c_{s,-,h}^2 &= c_s^2(\phi_{\mathrm{min}}, \chi_{\mathrm{min}}, \zeta(T_{h,n})T_{h,n}, T_{h,n}),
\end{aligned} \qquad (4.10)$$

where the arguments of $c_{s,+,v}^2$ etc. are as defined in Eq. (4.8). Thus, e.g., $c_s^2(\phi_{\mathrm{min}}, 0, T_n, \xi(T_n)T_n)$ denotes the velocity of the sound wave traveling inside the bubble of the visible phase transition. The visible scalar field is in its broken vacuum while the hidden scalar field is still in its symmetric vacuum. The tunneling temperature of the visible scalar field nucleation is T_n and the synchronous temperature of the hidden scalar to it is $\xi(T_n)T_n$.

On the other hand, when $T_n < \zeta(T_{h,n})T_{h,n}$, these four velocities are given by

$$\begin{aligned}
c_{s,+,h}^2 &= c_s^2(0, 0, \zeta(T_{h,n})T_{h,n}, T_{h,n}),\\
c_{s,-,h}^2 &= c_s^2(0, \chi_{\mathrm{min}}, \zeta(T_{h,n})T_{h,n}, T_{h,n}),\\
c_{s,+,v}^2 &= c_s^2(0, \chi_{\mathrm{min}}, T_n, \xi(T_n)T_n),\\
c_{s,-,v}^2 &= c_s^2(\phi_{\mathrm{min}}, \chi_{\mathrm{min}}, T_n, \xi(T_n)T_n).
\end{aligned} \qquad (4.11)$$

B. Relativistic fluid equations and bubble dynamics

Next, we discuss hydrodynamics of the bubble expansion [6,9,70–73]. First, we describe the plasma, as a relativistic fluid, by its energy-momentum tensor

$$T^{\mu\nu} = wu^\mu u^\nu + pg^{\mu\nu}. \qquad (4.12)$$

Here we are using the metric $g^{\mu\nu} = \mathrm{diag}(-1, 1, 1, 1)$ where $w = e + p$, and e and p are the energy density and pressure as defined in Sec. IV A, and $u^\mu = \gamma(v)(1, \vec{v})(\gamma = 1/\sqrt{1-v^2})$ is the four-velocity field. The fluid equation of motion is given by the conservation of $T^{\mu\nu}$,

$$\partial_\mu T^{\mu\nu} = \mu^\nu \partial_\mu(u^\mu w) + u^\mu w\partial_\mu u^\nu + \partial^\nu p = 0. \qquad (4.13)$$

The conservation equation can be projected into the parallel and perpendicular directions to the flow direction by using $u^\mu = \gamma(v)(1, \vec{v})$ and $\bar{u}^\mu = \gamma(v)(v, \vec{v}/v)$ such that $\bar{u}_\mu u^\mu = 0, u_\nu \partial_\mu u^\nu = 0, \bar{u}^2 = 1, u^2 = -1$ which give

$$u_\nu \partial_\mu T^{\mu\nu} = \partial_\mu(u^\mu w) + u^\mu \partial_\mu p = 0, \qquad (4.14)$$

$$\bar{u}_\nu \partial_\mu T^{\mu\nu} = \bar{u}_\nu u^\mu w\partial_\mu u^\nu + \bar{u}^\mu \partial_\mu p = 0. \qquad (4.15)$$

These are the continuity equation and the relativistic Euler equation. Further, one assumes a spherically symmetric configuration and since there is no characteristic distance scale in the problem, the solution depends only on a self-similarity coordinate $\eta \equiv r/t$, where r is the distance to the bubble center and t is the time since the bubble nucleation. Further, we assume that the bubble reaches a constant terminal velocity after a short expansion time. Thus, we can assume that $v_b = \eta_w$. The above two equations then take the form

$$(\eta - v)\frac{\partial_\eta e}{w} = 2\frac{v}{\eta} + \gamma^2(1 - \eta v)\partial_\eta v, \qquad (4.16)$$

$$(1 - \eta v)\frac{\partial_\eta p}{w} = \gamma^2(\eta - v)\partial_\eta v, \qquad (4.17)$$

where $v(\eta)$ is the fluid velocity at $r = \eta t$ in the frame of the bubble center. Using the definition $c_s^2 = \frac{dp/dT}{de/dT}$, one gets the following equations:

$$2\frac{v}{\eta} = \gamma^2(1 - v\eta)\left(\frac{\mu(\eta, v)^2}{c_s^2} - 1\right)\frac{dv}{d\eta}, \qquad (4.18)$$

$$\frac{dw}{d\eta} = w\gamma^2\mu(\eta, v)\left(\frac{1}{c_s^2} + 1\right)\frac{dv}{d\eta}, \qquad (4.19)$$

where $\mu(\eta, v) = \frac{\eta - v}{1 - \eta v}$. In fact, with a steady terminal velocity η_w, we can use this Lorentz-boost transformation to transform between the bubble wall frame and center of the bubble frame by the expressions $\mu(\eta_w, v) = \bar{v}$ and $\mu(\eta_w, \bar{v}) = v$. In addition to the equations of motion of the plasma given above, we also need junction conditions to connect the symmetry phase and the broken phase. We use subscripts $+$ to denote the symmetric phase and $-$ to denote the broken phase. We note that the junction conditions are to be used infinitely close to the boundary. Then assuming the wall is expanding in the z direction, the matching equations are

$$(T_+^{z\nu} - T_-^{z\nu})n_\nu = 0, \quad (T_+^{t\nu} - T_-^{t\nu})n_\nu = 0, \quad n_\mu = (0,0,0,1) \qquad (4.20)$$

and we get the continuity equation in the bubble wall frame to be

$$w_+\bar{v}_+\bar{\gamma}_+^2 = w_-\bar{v}_-\bar{\gamma}_-^2, \qquad (4.21)$$

$$w_+\bar{v}_+^2\bar{\gamma}_+^2 + p_+ = w_-\bar{v}_-^2\bar{\gamma}_-^2 + p_-. \qquad (4.22)$$

Rearranging it, we can get the following equation:

$$\bar{v}_+\bar{v}_- = \frac{p_+ - p_-}{e_+ - e_-}, \qquad (4.23)$$

$$\frac{\bar{v}_+}{\bar{v}_-} = \frac{e_- + p_+}{e_+ + p_-}. \qquad (4.24)$$

With boundary conditions (4.23) and (4.24) and the evolution equation (4.18), we can solve for $v(\eta)$, and there are three different expansion modes: deflagration, hybrid, and detonation. If the wall velocity of the bubble v_w is subsonic, i.e., $v_w < c_{s,-}$, it gives rise to deflagration where a region of larger density precedes the bubble wall. For the supersonic case where $v_w > c_{s,-}$, the higher density region ahead of the wall does not materialize since the wall velocity is larger than the sound velocity. This is the detonation region. The region where $v_w \sim c_s$ is a mixture of the two and is referred to as the hybrid region. Once we determine $v(\xi)$ we can apply Eqs. (4.19) and (4.21) to find

$$w(\eta) = w_0 \exp\left[\int_{v_0}^{v(\eta)}\left(1 + \frac{1}{c_s^2}\right)\gamma^2\mu dv\right]. \qquad (4.25)$$

The ratio of bulk kinetic energy over the vacuum energy gives the efficiency factor κ as

$$\kappa = \frac{3}{\epsilon\eta_w^3}\int w(\eta)v^2\gamma^2\eta^2 d\eta.$$

In most analyses of first-order phase transition (FOPT), sound velocities are treated approximately often assuming $c_{s,-}^2 = c_{s,+}^2 = \frac{1}{3}$ (see, e.g., [70,71]). In this case, the phase transition strength α is given by

$$\alpha = \frac{T\frac{d\Delta V_{\text{eff}}}{dT} - \Delta V_{\text{eff}}}{\rho_{\text{rad}}} \qquad (4.26)$$

or

$$\alpha' = \frac{4}{3}\frac{\epsilon_+ - \epsilon_-}{w_+} = \frac{\frac{T}{4}\frac{d\Delta V_{\text{eff}}}{dT} - \Delta V_{\text{eff}}}{\rho_{\text{rad}}}. \qquad (4.27)$$

However, in this work we will take into account sound velocity dependence in the analysis as in [74,75]. Here the phase transition strength parameter is given by

$$\alpha_{\bar{\theta}_n} \equiv \frac{D\bar{\theta}(T_n)}{3w_n} \qquad \bar{\theta} \equiv e - \frac{p}{c_{s,-}^2}, \qquad (4.28)$$

$$DX(T_n) = X_s(T_n) - X_b(T_n), \qquad (4.29)$$

with $X = e, p, w$ and the efficiency factor is defined by

$$\kappa = \frac{4}{\alpha_{\bar{\theta}_n}\eta_w^3}\int d\eta\eta^2 v^2\gamma^2\frac{w}{w_n}. \qquad (4.30)$$

In this case $\alpha_{\bar{\theta}_n}$ and κ are both velocity dependent, in that κ depends on $c_{s,+}, c_{s,-}, \alpha_{\bar{\theta}_n}$ and v_w. We note that for the case $c_{s,+}^2 = c_{c,b}^2 = 1/3$, it is equivalent to the second definition, Eq. (4.27). A Python snippet is provided in [74] and we utilize it in our analysis.

V. GRAVITATIONAL WAVE SPECTRUM WITH VISIBLE AND HIDDEN SECTORS

The phase transition phenomena is controlled by four parameters, which are the nucleation temperature T_n, the strength of the phase transition α, the inverse duration of the transition β in comparison with H_n where H_n is the Hubble parameter at the time of nucleation and the bubble wall velocity v_w. T_n and α were discussed in Sec. IV. The timescale of the phase transition is the inverse of the parameter β defined by

$$\beta = -\frac{d(S_3/T)}{dt}\bigg|_{t=t_n} \simeq \frac{1}{\Gamma}\frac{d\Gamma}{dt}\bigg|_{t=t_n}, \qquad (5.1)$$

where S_3 is the Euclidean action as already defined. Usually β is normalized by H_n and is given by

$$\frac{\beta}{H} = T \frac{d(S_3(T)/T)}{dT}\bigg|_{T=\{T_n,T_{h,n}\}}. \quad (5.2)$$

We note here that a larger α means a stronger phase transition and a larger value of β means a faster phase transition.

The gravitational wave power spectrum has been discussed in a variety of settings (see, e.g., [31,36,71,76–88]). It is given by

$$\Omega_{GW}(f) = \frac{1}{\rho_c}\frac{d\rho_{GW}}{d\ln f} \simeq \mathcal{N}\Delta\left(\frac{\kappa\alpha}{1+\alpha}\right)^p \left(\frac{H}{\beta}\right)^q s(f),$$

$$\Omega_{GW} \simeq \Omega_\phi + \Omega_{sw} + \Omega_{tb}. \quad (5.3)$$

Here Ω_ϕ is the contribution to energy density of the gravitational wave produced by dynamics of the scalar field, Ω_{sw} is the contribution from the sound waves, Ω_{tb} is the contribution by turbulence, ρ_c is the critical density, and f is the frequency of the gravitational wave. The rest of the parameters are as discussed in the text of this section. Further, a detailed discussion of the various contributions can be found in [52,89–92]. For the current analysis, all the relevant parameters that enter in the computation of $\Omega_\phi, \Omega_{sw}, \Omega_{tb}$ which contribute in Eq. (5.3) are given in Table I. However, we still need to consider the redshift both on the energy density and frequency to deduce the power spectrum $\Omega_{GW}^0(f_0)$ at current temperature T^0 from the power spectrum Ω_{GW} gotten at the tunneling temperature T_{tun}. This is accomplished by the following extrapolation [36,52]:

$$\Omega_{GW}^0(f_0) = \mathcal{R}\,\Omega_{GW}\left(\frac{a_0}{a}f_0\right), \quad (5.4)$$

where

TABLE I. Values of the parameters $\mathcal{N}, \kappa, p, q, \Delta, f_p, s(f)$ that appear in the gravitational wave power spectrum of Eq. (5.3) for the three different contributions: Ω_ϕ from the scalar field, Ω_{sw} from sound waves, and Ω_{tb} from turbulence.

	Scalar field Ω_ϕ	Sound waves Ω_{sw}	Turbulence Ω_{turb}
$\mathcal{N}$	1	1.59×10^{-1}	2.01×10^{1}
κ_ϕ	κ	κ_{sw}	$\epsilon_{turb}\kappa_{sw}$
p	2	2	$\frac{3}{2}$
q	2	1	1
Δ	$\frac{0.11 v_w^3}{0.42+v_w^2}$	v_w	v_w
f_p	$\frac{0.62\beta}{1.8-0.1v_w+v_w^2}$	$\frac{2\beta}{\sqrt{3}v_w}$	$\frac{3.5\beta}{2v_w}$
$s(f)$	$\frac{3.8(f/f_p)^{2.8}}{1+2.8(f/f_p)^{3.8}}$	$(f/f_p)^3\left(\frac{7}{4+3(f/f_p)^2}\right)^{7/2}$	$\frac{(f/f_p)^3}{(1+f/f_p)^{11/3}(1+8\pi f/H)}$

$$\frac{a_0}{a} = \left(\frac{h_{eff}(T_{tun})}{h_{eff}^{EQ}}\right)^{1/3}\left(\frac{T_{tun}}{T^0}\right), \quad (5.5)$$

$$\mathcal{R} \equiv \left(\frac{a}{a_0}\right)^4 \left(\frac{H}{H_0}\right)^2$$

$$\simeq 2.473 \times 10^{-5} h^{-2}\left(\frac{h_{eff}^{EQ}}{h_{eff}(T_{tun})}\right)^{4/3}\left(\frac{g_{eff}(T_{tun})}{2}\right), \quad (5.6)$$

$$g_{eff}(T_{tun}) = g_{eff}^v(T_{tun}) + g_{eff}^h(T_{tun})\xi(T_{tun})^4, \quad (5.7)$$

$$h_{eff}(T_{tun}) = h_{eff}^v(T_{tun}) + h_{eff}^h(T_{tun})\xi(T_{tun})^3, \quad (5.8)$$

$$h_{eff}^{EQ} = 3.91 + h_{eff}^h(T_{eq})\xi(T_{eq})^3. \quad (5.9)$$

In the above $T_{tun} = T_n$ for the visible sector nucleation and $T_{tun} = \zeta(T_{h,n})T_{h,n}$ for the hidden sector nucleation.

It is also necessary to classify whether the bubble wall velocity reaches a terminal velocity. If the bubble wall keeps accelerating, it is called the runaway scenario. If it reaches a terminal velocity, it is called a nonrunaway scenario. A detailed discussion can be found in [52,70,92,93]. To classify these two scenarios, a critical phase transition strength α_∞ is introduced. For the visible sector and hidden sector nucleation, it is given by

$$\alpha_\infty^v = \frac{(T_n)^2}{\rho_{rad}(T_n)}\left(\sum_{i=bosons} n_i\frac{\Delta m_i^2}{24} + \sum_{i=fermions} n_i\frac{\Delta m_i^2}{48}\right), \quad (5.10)$$

$$\alpha_\infty^h = \frac{(T_{h,n})^2}{\rho_{rad}(\zeta(T_{h,n})T_{h,n})}\left(\sum_{i=bosons} n_i\frac{\Delta m_i^2}{24} + \sum_{i=fermions} n_i\frac{\Delta m_i^2}{48}\right). \quad (5.11)$$

When $\alpha_\infty > \alpha$, it is in the nonrunaway regime. In this case, we have

$$\kappa_\phi = 0, \qquad \kappa_{sw} = \kappa(\alpha, c_{s,+}^2, c_{s,-}^2, v_w). \quad (5.12)$$

When $\alpha_\infty < \alpha$, it is in the runaway regime and we have

$$\kappa_\phi = 1 - \frac{\alpha_\infty}{\alpha}, \qquad \kappa_{sw} = \frac{\alpha_\infty}{\alpha}\kappa(\alpha_\infty, c_{s,+}^2, c_{s,-}^2, v_w). \quad (5.13)$$

The bubble wall velocity depends on the transition strength α and on the friction between the scalar field and the surrounding particle plasma, described by a friction parameter. Thus, v_w is highly model dependent. Since the bubble wall is in the runaway region, it will keep accelerating, and for that reason we take $v_w \sim 1$. In the nonrunaway region, the bubble wall velocity reaches a terminal value and is model dependent, so we treat it as a free parameter. It is legal to do so since it is equivalent to introducing additional particles that couple exclusively to
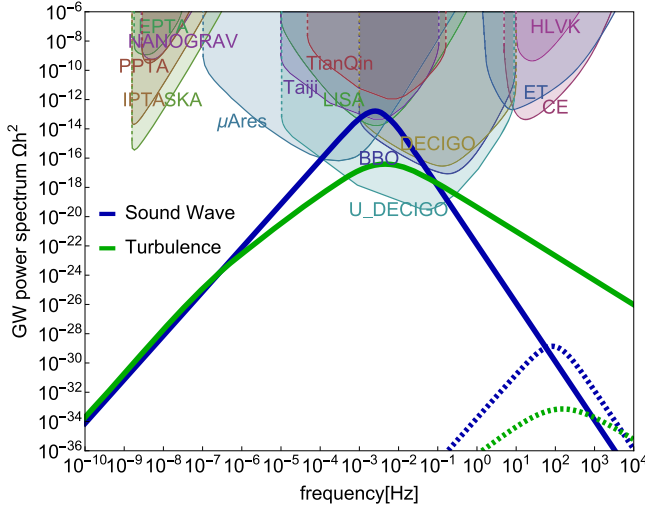
FIG. 3. An exhibition of the gravitational wave power spectrum for model (a) in Table II illustrating the relative contributions from sound wave and turbulence. This is a nonrunaway case and $\Omega_\phi = 0$. The solid lines are for the hidden sector phase transition while the dashed lines are for the visible sector. In the analysis we take $\epsilon_{\text{turb}} = 0.1$ as in [90,92]. The regions in color are the power-law integrated sensitivity curves for different experiments, including LISA [96–98], EPTA [99,100], HLVK = aLIGO/aVIRGO/KAGRA [101–106], BBO [107], DECIGO [108], ET [109], CE [110], Taiji [111], TianQin [112], μAres [113], NANOGrav [114,115], PPTA [116], IPTA [117], and SKA [118]. The data and calculations are from [119].

the scalar field and affect the friction parameter only (for recent work on determining wall velocity from initial inputs see, e.g., [74,75,94,95]).

VI. SIMULATION OF GRAVITATIONAL WAVE POWER SPECTRUM

There are several ongoing gravitational wave experiments and those being proposed that will probe gravitational waves at different frequency regions and with different sensitivity. These include Laser Interferometer Space Antenna (LISA) [96–98], EPTA [99,100], aLIGO/aVIRGO/KAGRA

[101–106], BBO [107], DECIGO [108], Einstein Telescope (ET) [109], Cosmic Explorer (CE) [110], Taiji [111], TianQin [112], μAres [113], NANOGrav [114,115], Parkes Pulsar Timing Array (PPTA) [116], International Pulsar Timing Array (IPTA) [117], and Square Kilometer Array (SKA) [118]. We plot the predictions of the hidden sector model discussed here along with the expected reach of proposed gravitational wave experiments. Figure 3 provides an example of gravitational wave power spectrum with these experimental constraints for model (a) of Table II. Since the major parameters for the standard model (SM) are already known, we have the visible sector nucleation temperature to be about 161.284 GeV, the phase transition strength $\alpha_v \sim 4 \times 10^{-5}$, and the inverse duration of the transition $\beta_v \sim 2.7 \times 10^6$. As a result, the direct contribution from the visible sector is very small, which is about $\Omega_{\text{visible}} h^2 \sim 10^{-30}$.

Based on the previous discussion, we calculate the phase transition dynamics and the final gravitational wave power spectrum with different benchmarks on our model. For each model, there are eight free parameters in total, which are dark fermion mass m_D, dark photon mass $m_{\gamma'}$, coupling of dark photon and dark fermion g_x, kinetic mixing δ, initial temperature ratio ξ_0, hidden Higgs field parameter μ_h, λ_h, and the bubble wall velocity for hidden sector nucleation v_{wh}. Here we provide a table of benchmark models in Table II with their outputs given in Table III.

A. Constraints and Monte Carlo simulation

In the beginning of this section we discussed eight parameters that enter in the analysis of the gravitational wave spectrum. For simulations we take the following ranges for these parameters:

$$m_D \in (10^{-1}, 10^4) \text{ GeV}, \qquad m_{\gamma'} \in (10^{-1}, 10^4) \text{ GeV},$$
$$g_x \in (10^{-4}, 10^0), \qquad \delta \in (10^{-12}, 10^{-6}),$$
$$\xi_0 \in (0, 1), \qquad \mu_h \in (10^{-1}, 10^4) \text{ GeV},$$
$$\lambda_h \in (10^{-5}, 10^1), \qquad v_{\text{wh}} \in (0, 1). \tag{6.1}$$

TABLE II. A set of benchmarks covering a range of input parameters used in the computation of tunneling temperature in the hidden sector and other relevant outputs in Table III that enter in the computation of the gravitational wave spectrum consistent with all constraints on the dark photon [120]. These benchmarks pass all the constraints mentioned in Sec. VI A and are cosmologically consistent candidate models for the computation of gravitational waves.

Number	m_D (GeV)	$m_{\gamma'}$ (GeV)	g_X	δ (in 10^{-9})	ξ_0	μ_h (GeV)	λ_h	v_{wh}
(a)	551.7	108.5	0.02059	0.01038	0.671	18.63	0.04973	0.5993
(b)	204.1	52.52	0.01975	0.01441	0.463	9.922	0.03953	0.5619
(c)	594.4	221.5	0.002922	0.0281	0.778	41.78	0.08802	0.9599
(d)	710	138.6	0.003161	0.03012	0.917	22.03	0.02939	0.6472
(e)	1111	113.7	0.02739	0.01174	0.821	18.49	0.03857	0.2674
(f)	2854	249.5	0.00821	0.03464	0.795	41.44	0.04183	0.5871
(g)	530.7	124.7	0.04001	0.02102	0.757	17.14	0.01621	0.6159

TABLE III. Computation of the nucleation temperature $T_{h,n}$, sound velocities in the symmetric and broken phases $c^2_{s,+,h}, c^2_{s,-,h}$, the strength of the phase transition α_h, the inverse duration of the transition β_h/H_n, and the efficiency factor κ_h all for the hidden sector. Also listed is the dark matter relic density $\Omega_{DM}h^2$, frequency $f(z)$ of the power spectrum at the peak value of the gravitational wave power spectrum, and the gravitational wave power spectrum $\Omega_{GW}h^2$ at peak value. DET, HYB, and DEF stand for the nucleation modes detonation, hybrid, and deflagration.

Number	$T_{h,n}$	$\xi(T_n)$	$c^2_{s,+,h}$	$c^2_{s,-,h}$	α_h	β_h/H_n	κ_h	$\Omega_{DM}h^2$	f[Hz]	$\Omega_{GW}h^2$	Mode
(a)	18.2	0.6724	0.307	0.306	0.0172	294.8	0.223	0.013	0.00257	1.591×10^{-13}	HYB
(b)	18.02	0.4635	0.309	0.309	0.00053	1563.	0.0463	0.0267	0.0204	1.172×10^{-18}	HYB
(c)	29.93	0.7794	0.309	0.308	0.043	158.8	0.0523	0.0198	0.0012	1.524×10^{-13}	DET
(d)	35.52	0.9181	0.308	0.306	0.0151	871.3	0.0984	0.0385	0.0102	8.604×10^{-15}	DET
(e)	19.73	0.8227	0.309	0.308	0.0367	319.7	0.0413	0.0115	0.0055	9.823×10^{-15}	DEF
(f)	54.78	0.7956	0.318	0.317	0.0107	845.6	0.187	0.0228	0.0191	1.42×10^{-14}	HYB
(g)	28.07	0.758	0.308	0.307	0.0127	565.9	0.175	0.0216	0.00631	2.843×10^{-14}	HYB

In order to investigate the distribution of different nucleation modes, as discussed in Sec. VI C, for each event we select v_{wh} corresponding to three different nucleation modes so that the total number for each type of mode is the same. In the Monte Carlo simulation we impose the following constraints:

(1) FOPT constraints: For the first-order phase transition, we require that there must be a potential barrier between the false vacuum and the true vacuum. The further constraint is an upper limit of sound velocity so that $c_s^2 \leq 1/3$.

(2) ΔN_{eff} constraint at BBN: The number of effective relativistic degrees of freedom N_{eff} at BBN is one of the important constraints on new physics beyond the standard model of particle physics. The relevant constraint is given by the allowed corridor for the difference between the experimental result and the standard model result at the BBN time represented by ΔN_{eff}. For the hidden sector model the extra degrees of freedom are given by

$$\Delta N_{eff} = \frac{4}{7} g^h_{eff} \left(\frac{11}{4}\right)^{4/3} \xi^4. \quad (6.2)$$

Current experiment observations give us the constraint $\Delta N_{eff} < 0.25$ [121].

(3) Relic density constraint: After solving for the yield equations, the relic densities for χ and D can be gotten from their individual yields so that

$$\Omega_i h^2 = \frac{\mathbf{s}_0 m_i Y^0_i h^2}{\rho_c}, \qquad i \in (D, \chi), \quad (6.3)$$

where Y^0_i is the yield for the ith particle and $\Omega_i h^2$ is its relic density, while the total relic density is the sum of them. In the analysis we use dark matter relic density as an upper limit. Currently, it is given by the Planck experiment [121] so that

$$\Omega_{DM} h^2 = 0.120 \pm 0.001. \quad (6.4)$$

Specifically, we impose the constraint $0.01 < \Omega_{hidden} h^2 < 0.12$.

For each benchmark model, there will be a corresponding power spectrum curve just like Fig. 3. However, plotting the full curve for each model point would not be illuminating because they would be space filling. For that reason we will do a scatter plot on the gravitational wave power spectrum, with each model point represented by the peak of its power spectrum curve at the frequency where that peak occurs. An illustration of it is given in Fig. 4.

B. Nucleation temperature and GW power spectrum

Nucleation temperature is one of the key factors in the computation of the gravitational wave power spectrum. It affects the spectrum in the following ways:

(1) It enters the phase transition strength α as discussed below

$$\alpha = \frac{\epsilon}{\rho_{rad}}. \quad (6.5)$$

Although there are several different definitions to the latent heat ϵ as discussed earlier, the total radiation density of the Universe ρ_{rad} is the same and is given by

$$\rho_{rad} = \frac{\pi^2}{30} (g^v_{eff}(\zeta T_{h,n}) T_{h,n}^4 \zeta^4 + g^h_{eff}(T_{h,n}) T_{h,n}^4). \quad (6.6)$$

It tells us that $\alpha \propto T_{h,n}^{-4}$. Thus, a smaller $T_{h,n}$ leads to a larger α and a larger gravitational wave power spectrum.

(2) According to Eq. (5.4), we have $f_0 \propto T_{h,n}$, which implies that a larger power spectrum will arise at lower frequencies.

The analysis of Fig. 4 is consistent with the observation above that a larger power spectrum will appear at a lower frequency. We also note that, for the two-field case,
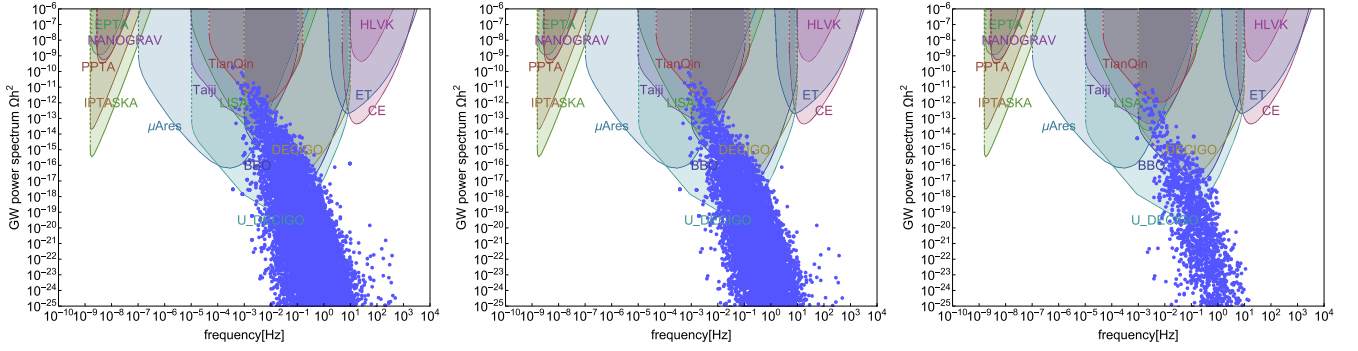
FIG. 4.   Gravitational wave power spectrum resulting from Monte Carlo analysis on eight free parameters. Left: scatter plot of the peak value of candidate models at the frequency where the peak value occurs after FOPT constraints are applied. Middle: same as the left panel including FOPT constraints and the ΔN_{eff} constraint. Right: same as the left panel including the FOPT constraints, ΔN_{eff} constraint, and the relic density constraint.
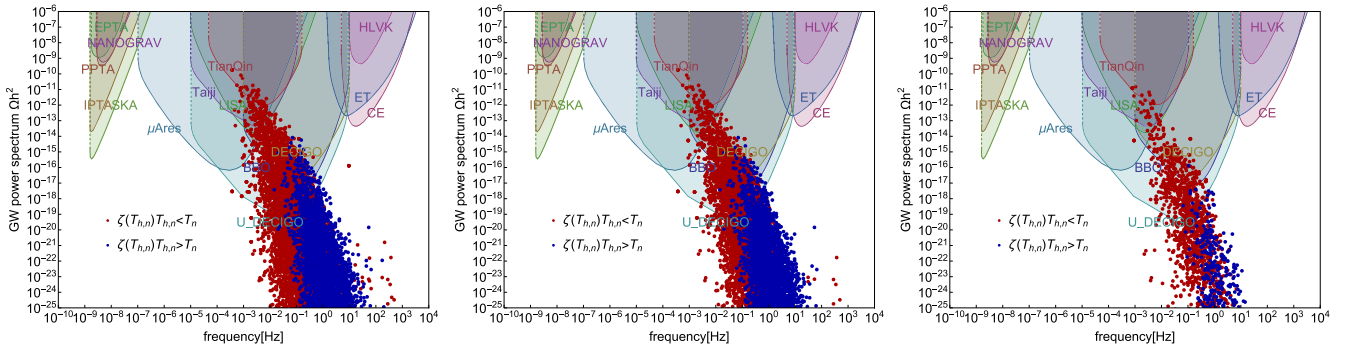

FIG. 5.   Monte Carlo analysis of gravitational wave power spectrum classified by two possible orderings in which nucleation occurs in the visible and hidden sector with red model points for $T_n > \zeta(T_{h,n})T_{h,n}$ and blue model points for $\zeta(T_{h,n})T_{h,n} > T_n$. Left: scatter plot of the candidate models satisfying the FOPT constraints. Middle: same as the left panel satisfying the FOPT constraints and the ΔN_{eff} constraint. Right: same as the left panel with models satisfying the FOPT constraints, ΔN_{eff} constraint, and the relic density constraint. Here one finds that the residual set of models left after all the constraints are applied are those where the nucleation in the hidden sector happens after nucleation in the visible sector.

satisfaction of FOPT and other constraints is affected by the order in which nucleation in the visible and in the hidden sector occurs. Thus, we classify all FOPT events into two groups: (1) the standard model Higgs scalar nucleation happens first, i.e., $\zeta(T_{h,n})T_{h,n} < T_n$ (red points) or (2) the hidden Higgs scalar nucleation happens first, i.e., $\zeta(T_{h,n})T_{h,n} > T_n$ (blue points). The analysis for these two cases is shown in Fig. 5. Here the analysis shows that after the FOPT constraints, ΔN_{eff} constraint, and the relic density constraint are taken into account most of the blue points are eliminated, which implies that the hidden sector nucleation occurs after nucleation in the visible sector.

C. Sound velocity and GW power spectrum

We discussed above the effect of sound velocity on the final power spectrum via $\alpha(c^2_{s,-,h})$ according to Eq. (4.28) and via $\kappa(\alpha, c^2_{s,+,h}, c^2_{s,-,h}, v_w)$ according to Eq. (4.30). To demonstrate to what extent sound velocity can change the power spectrum, we investigate the power spectrum for model (b) from Table II keeping all parameters fixed except

for the sound velocity $c^2_{c,b,h}$. The analysis of Fig. 6 shows that the changes to power spectrums can be as large as a factor of $\mathcal{O}(10^3)$. This approach allows us to isolate the effects of sound velocity from other factors, such as the nucleation temperature noted earlier. The reason we need to discuss this dependence is because there are multiple different analyses on sound velocity among existing works that lead to different results. We classify these as follows:

(A) This is the case when one considers just the hidden sector and assumes that the sound velocity takes its maximum value allowed in fluids which is $c^2_s = 1/3$. Such an assumption is the one most commonly made, see, e.g., [52,122].

(B) Here one considers one hidden sector model but including sound velocity dependence. For this class of models α is given by Eq. (4.28) and κ will also be velocity dependent. The sound velocity is given by

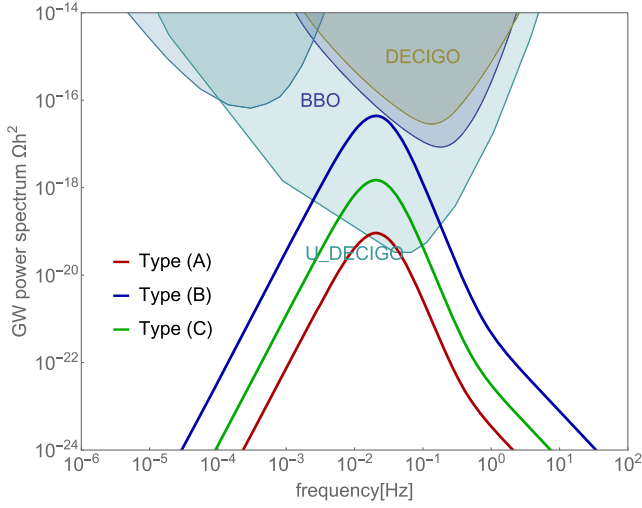$$c^2_s = \frac{dp_h/dT_h}{de_h/dT_h}, \qquad (6.7)$$

FIG. 6. An exhibition of the gravitational wave power spectrum for different types of sound velocities for a example model. All other parameters, such as the nucleation temperature, are kept fixed when $c_{s,-,h}^2$ varies for cases A, B, and C discussed in the text.

where p_h and e_h are the pressure and the energy density for the hidden sector. Analyses of this type are discussed in, for example, [74,123].

(C) In this work, we discuss sound velocity involving two sectors, i.e., the visible and the hidden, and take into account velocity dependence, which is given by Eq. (4.8). This type of analysis has not been discussed in the existing literature to our knowledge.

Applying the above three types of analyses (A)–(C) to model (b), we get sound velocities such that $c_{s,-,h,(A)}^2 = 0.333, c_{s,-,h,(B)}^2 = 0.234, c_{s,-,h,(C)}^2 = 0.309$. Correspondingly, the gravitational wave power spectrum for the three cases is significantly affected due to variations in the sound velocity as illustrated in Fig. 6.

D. Nucleation temperature and sound velocity

In this section, we will analyze how the sound velocity depends on the nucleation temperature. Again, we will focus on $c_{s,-,h}^2$, with sound velocity defined as by Eq. (4.8).

The scatter plot is shown in Fig. 7. We observe that some of the points in Fig. 7 are gathered around the curve of $c_s^2 = \frac{d(p_v)/dT}{d(e_v)/dT}$. This phenomenon happens because the visible sector dominates, i.e., we have the sound velocity so that

$$c_s^2(\phi,\chi,T,T_h) = \frac{d(p_v+p_h)/dT}{d(e_v+e_h+e_{\mathrm{mix}})/dT} \simeq \frac{d(p_v)/dT}{d(e_v)/dT}. \quad (6.8)$$

The reason that the visible sector can dominate is because $p_v \sim \frac{\pi^2}{90} g_{\mathrm{eff}}^v T^4$ and $p_h \sim \frac{\pi^2}{90} g_{\mathrm{eff}}^h T_h^4$ according to Eqs. (4.3), (4.4) and $T > T_h$ when $\xi < 1$ and also $g_{\mathrm{eff}}^v > g_{\mathrm{eff}}^h$.

One may note from Fig. 7 that, for the case when the hidden Higgs scalar nucleation occurs first, i.e., $\zeta(T_{h,n})T_{h,n} > T_n$, the red curve stays at $c^2 \sim 1/3$. However, when the standard model Higgs scalar nucleation occurs first, i.e., $T_n > \zeta(T_{h,n})T_{h,n}$, we have c_s^2 systematically less than $1/3$. The different behavior for the two cases arises due to two different constraints, i.e., Eqs. (4.10) and (4.11), for these two different cases. In the analysis of Sec. VI B, it is found that most of events that pass all the relevant constraints are those where $T_n > \zeta(T_{h,n})T_{h,n}$ and where the approximation $c_s^2 \sim 1/3$ is typically invalid. In simple terms the cosmologically preferred model points are those where $T_n > \zeta(T_{h,n})T_{h,n}$ and $c_s^2 < 1/3$.

1. ΔN_{eff} vs $\xi(T)$

According to Eq. (6.6), the hidden sector nucleation happens at $T_{h,n}$ which lies in the range 18–55 GeV according to Table III, while the BBN temperature is $O(1)$ MeV. This means we need to extrapolate the N_{eff}
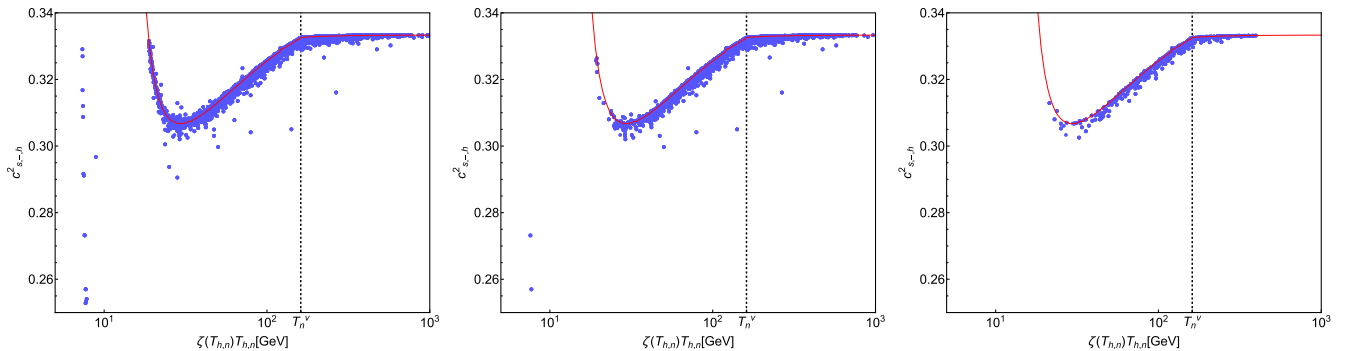

FIG. 7. Scatter plots for $c_{s,-,h}^2$ vs $\zeta(T_{h,n})T_{h,n}$ for a set of candidate models in the parameter ranges given by Eq. (6.1). Here the standard model dominates over the hidden sector in the computation of sound velocity and the sound velocity is close to the one for the visible sector, i.e., $c_s^2 = \frac{d(p_v)/dT}{d(e_v)/dT}$ shown by the red curve. The vertical black lines give the value of T_n. Left: scatter plot of $c_{s,-,h}^2$ vs $\zeta(T_{h,n})T_{h,n}$ with inclusion of FOPT constraints. Middle: same as the left panel including the FOPT constraints and the ΔN_{eff} constraint. Right: same as the left panel with FOPT constraints, ΔN_{eff} constraint, and the relic density constraint.
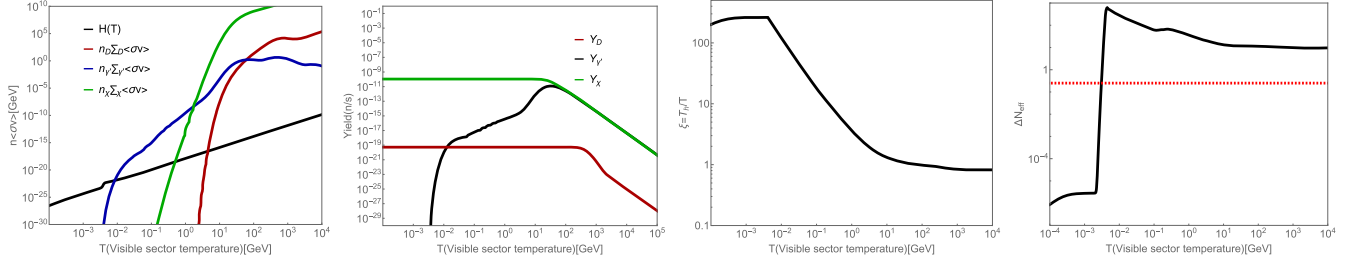
FIG. 8. Left: an exhibition of the decouplings of hidden sector particles with plots of $n_i \sum_i \langle \sigma v \rangle$ and $H(T)$ vs T for $i = D, \gamma', \chi$. Here we have $n_D \sum_D \langle \sigma v \rangle = n_D(\langle \sigma v \rangle_{D\bar{D} \to i\bar{i}} + \langle \sigma v \rangle_{D\bar{D} \to \gamma'\gamma'})$, $n_{\gamma'} \sum_{\gamma'} \langle \sigma v \rangle = n_{\gamma'}(\langle \sigma v \rangle_{D\bar{D} \to \gamma'\gamma'} + \langle \sigma v \rangle_{\chi\bar{\chi} \to \gamma'\gamma'} + \langle \Gamma_{\gamma' \to i\bar{i}}(T_h) \rangle + \langle \Gamma_{\chi \to \gamma'\gamma'}(T_h) \rangle)$, $n_\chi \sum_\chi \langle \sigma v \rangle = n_\chi(\langle \sigma v \rangle_{\chi\bar{\chi} \to \gamma'\gamma'} + \langle \Gamma_{\chi \to \gamma'\gamma'}(T_h) \rangle)$. Left middle: an exhibition of the decay of dark photon γ'. The dark photon decays out at about 10^{-3} GeV. Right middle: evolution of $\xi(T)$ vs T for model (e) of Table II. Right: $\Delta N_{\text{eff}}(T)$ vs T. The red dashed line is the current limit $\Delta N_{\text{eff}} < 0.25$.

between the two temperatures in a precise way so as to take account of the ΔN_{eff} constraint at BBN time, which we take to be $\Delta N_{\text{eff}} < 0.25$. In some previous works separate entropy conservation in the visible and hidden sectors is used to extrapolate N_{eff} from high temperatures to low temperatures. Such a procedure is shown to be flawed as it can yield highly inaccurate estimates on ΔN_{eff}. Thus, a more accurate analysis is needed as discussed in Sec. II and Appendix E. An analysis relevant to the current case is given in Fig. 8. Here we first show that the two sectors decouple at 10^{-2} GeV and the dark photon also decays out at 10^{-2} GeV. The left panel exhibits the decoupling more clearly where $n_i \sum_i \langle \sigma v \rangle$ for all three hidden sector particles falls below $H(T)$ at $T \sim 10^{-2}$ GeV, which means the complete decoupling of the hidden and visible sectors (see Appendix E), and the density of dark relics freezes out as exhibited in the left-middle panel. The right-middle panel exhibits $\xi(T)$ vs T, which is used to constraint ΔN_{eff} at the BBN time as shown in the right panel. The right panel shows that ΔN_{eff} drops below the BBN constraint when decoupling happens.

E. Gravitational wave power spectrum and the nucleation modes: Detonation, deflagration, hybrid

Now we discuss the gravitational wave power spectrum for different nucleation modes: detonation, deflagration, and hybrid. Chapman-Jouguet velocity [72,73,124] is used in part to distinguish different bubble nucleation modes, specifically the detonation and the hybrid modes. It is given by [74,75]

$$v_J = \frac{1 + \sqrt{3\alpha_{\bar{\theta}}(1 - c_s^2 + 3c_s^2\alpha_{\bar{\theta}})}}{1/c_s + 3c_s\alpha_{\bar{\theta}}}. \quad (6.9)$$

The bubble nucleation modes are distinguished by the following constraints:

(1) Detonations: $v_w > c_{s,-}$ and $v_w > v_J$.
(2) Hybrid: $v_w > c_{s,-}$ and $v_w < v_J$.
(3) Deflagrations: $v_w < c_{s,-}$.

Here, v_w is the bubble wall velocity. We apply such classification to all data points in Monte Carlo analysis to produce Fig. 9. The figure shows that the hybrid modes are typically the ones with the highest power spectrum.
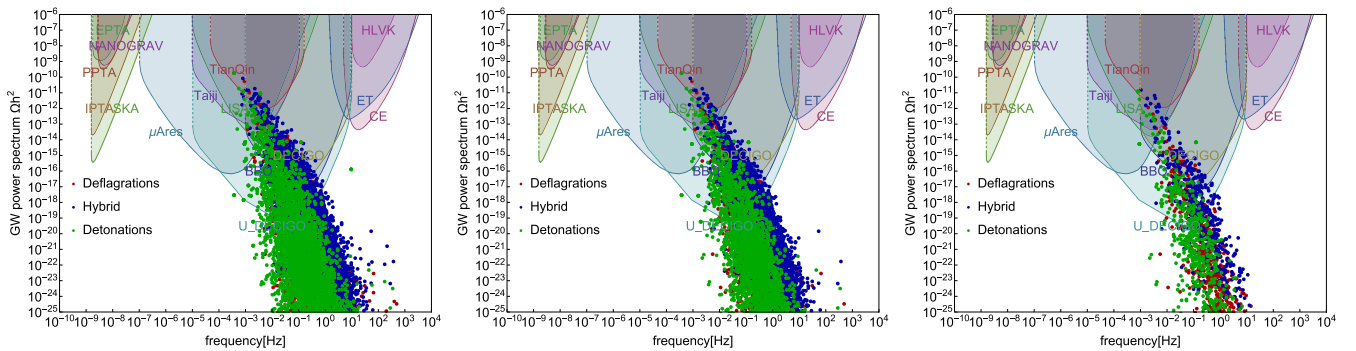

FIG. 9. Gravitational wave power spectrum for Monte Carlo analysis classified by different nucleation modes: detonation, deflagration, hybrid. Left: allowed set of models satisfying the FOPT constraints. Middle: same as the left panel with models satisfying FOPT constraints and the ΔN_{eff} constraint. Right: residual set of models satisfying the FOPT constraint, ΔN_{eff} constraint, and the relic density constraint.

VII. CONCLUSION

In this work we have carried out a cosmologically consistent analysis of gravity wave power spectrum arising from a first-order phase transition involving two sectors: the visible sector and the hidden sector, since the two sectors are intrinsically entangled in several ways. Thus, the Hubble expansion involves energy densities of all sectors, hidden and visible. Further, the strength of the first-order phase transition in the hidden sector at tunneling time $T_{h,n}$ depends on $\alpha(T_{h,n}) = \epsilon/\rho_{\rm rad}$ where ϵ is the latent heat and $\rho_{\rm rad} = \rho_{\rm rad}^h(T_{h,n}) + \rho_{\rm rad}^v(T)$ where $T = \zeta(T_{h,n})T_{h,n}$ and involves the evolution function $\zeta(T_h)$. The same evolution function enters when we impose the $\Delta N_{\rm eff}$ constraint at BBN time. Thus, imposition of $\Delta N_{\rm eff}$ at BBN requires a knowledge of the hidden sector temperature at BBN time which in the visible sector is ~1 MeV. Again one needs the evolution function to deduce the effective degrees of freedom in the hidden sector at the temperature synchronous to ~1 MeV in the visible sector. In brief, since the visible and the hidden sectors reside in different heat baths, a consistent analysis requires that one takes into account the dependence of the effective potential on two temperatures: one for the visible and the other for the hidden. In this work, we have presented an analysis of the gravitational wave power spectrum which takes into account the synchronous evolution of the visible and the hidden sectors. Within this framework we discuss nucleation which involves bubble dynamics in two sectors. The analysis involves a solution to the evolution function $\xi(T) = T_h/T$ along with a solution to yield equations for the hidden sector particles. Thus, the formalism discussed in this work allows one to correlate physics at nucleation time and at BBN time and allows for precision computation of $\Delta N_{\rm eff}$ at BBN and of relic density. The formalism presents an improvement over current analyses where synchronous evolution of the visible and the hidden sectors is not utilized.

Several aspects of the gravitational wave power spectrum are analyzed within the two temperature evolution formalism. Thus, we analyze the sensitivity of the gravitational wave power spectrum to sound speed for symmetric and broken phases. The analysis includes nucleation involving two fields, one from the hidden and the other from the visible. Here it is shown that, for the case two-field nucleation, models that pass all the constraints are those where the tunneling in the visible sector precedes tunneling in the hidden sector. Further, we discuss the possible imprint of the nucleation modes, i.e., detonation, deflagration, and hybrid on the characteristics of the gravitational power spectrum. We show that a part of the parameter space of the specific gauged $U(1)$ extension of the standard model discussed here is testable at the proposed gravitational wave detectors.

Finally, we mention below the novel material contained in the paper.

All the published works on gravitational wave production in hidden sector models thus far, that we are aware of, do not qualify as cosmologically consistent models since there is no synchronous thermal evolution of the visible and the hidden sectors in these works, and our work is the first one that has accomplished that. Details of how a synchronous evolution of the visible and the hidden sectors is achieved in a two sector/two temperature universe is discussed in detail in Secs. II–IV and in Appendixes A–E. Thus, currently this paper is the only cosmologically consistent model and no comparable analysis exists in the literature. This is reflected in the first three words of the title of this paper: "Cosmologically consistent analysis."

This paper is the first work where the imprint of different nucleation modes, i.e., detonation, deflagration, and hybrid, on the gravitational wave power spectrum is analyzed (see Fig. 9). This aspect of the paper is of great significance since it tells us that experimental data on gravitational waves can be used to probe the very early history of the Universe when the current Universe was in the process of creation via bubble formation. No comparable analysis exists in any of the previous works.

Among other novel things, in this work we discussed sound speeds involving two sectors (see Sec. IV), i.e., the visible and the hidden, which have a very significant effect on the gravitational power spectrum when both sound speeds are taken into account as seen in Fig. 6. Here the very large effect that inclusion of sound speeds of both the visible and of the hidden sector can generate on the power spectrum is exhibited. This type of analysis has not been discussed in the existing literature to our knowledge, and thus our analysis is more complete than what appears in the previous works for the two sector case.

Note added. Recently, the Ref. [125] appeared which uses dimensionally reduced 3D thermal field theory to minimize the uncertainty of the gravitational wave signal. This work along with those referenced in it are a useful tool in making the thermal analysis more precise. It is of interest to extend the analysis of this work to a two sector/two temperature case so as to be applicable to gravitational power spectrum involving the standard model and the hidden sector discussed in this work.

APPENDIX A: THERMAL MASS CALCULATION FOR A GENERAL $U(1)$ THEORY

We discuss here the calculation of thermal masses for the hidden sector Lagrangian given by Eqs. (2.2) and (2.4). The calculation is done in the high temperature regime,

where the temperature is much higher than the energy scale of the particles' masses. We also take all the external momenta to zero. In thermal field theory, at some nonzero temperature T, the 1PI graphs are defined in the Euclidean space ($t = i\tau$) with a periodicity in τ. The computations are governed by the conventional Feynman rules, while replacing the k^0 integral by a sum over Matsubara frequencies [126] so that

$$\int \frac{d^4k}{(2\pi)^4} f(k^0, \mathbf{k}) \to T\sum_n \int \frac{d^3\mathbf{k}}{(2\pi)^3} f(k^0 = i\omega_n, \mathbf{k}), \qquad \omega_n^b = 2n\pi T, \qquad \omega_n^f = (2n+1)\pi T, \tag{A1}$$

where ω_n^b is for bosonic modes and ω_n^f is for fermionic modes. For the rest of the calculation it is useful to define a function $q(T)$ so that

$$q(z) = 1 + \frac{2\varsigma}{e^{z/T} - \varsigma}, \tag{A2}$$

with $\varsigma = +1$ for bosons and $\varsigma = -1$ for fermions. Some of the integrals that appear in the thermal masses can then be given in terms of $\xi(z)$. Thus, we have

$$T\sum_n \int \frac{d^3\mathbf{k}}{(2\pi)^3} \frac{1}{\omega_n^2 + |\mathbf{k}|^2} = \int_0^\infty \frac{dk k^2}{2\pi^2} \frac{q(k)}{2k} = \begin{cases} T^2/12 & \text{bosons} \\ -T^2/24 & \text{fermions} \end{cases} \tag{A3}$$

$$T\sum_n \int \frac{d^3\mathbf{k}}{(2\pi)^3} \frac{\omega_n^2}{(\omega_n^2 + |\mathbf{k}|^2)^2} = \int_0^\infty \frac{dk k^2}{2\pi^2} \frac{k + 2Tq(k) - kq^2(k)}{8kT} = \begin{cases} -T^2/24 & \text{bosons} \\ T^2/48 & \text{fermions} \end{cases} \tag{A4}$$

$$T\sum_n \int \frac{d^3\mathbf{k}}{(2\pi)^3} \frac{|\mathbf{k}|^2}{(\omega_n^2 + |\mathbf{k}|^2)^2} = \int_0^\infty \frac{dk k^2}{2\pi^2} \frac{-k + 2Tq(k) + kq^2(k)}{8kT} = \begin{cases} T^2/8 & \text{bosons} \\ -T^2/16 & \text{fermions} \end{cases} \tag{A5}$$

where we dropped the nonthermal contribution in the integral which is UV divergent and is removed by the counterterms. There are no thermal corrections to the fermion masses, and only the scalar boson and the longitudinal components of the gauge boson gain thermal corrections.

1. Thermal mass correction to scalar χ

We discuss the thermal corrections to the scalar boson first. Here the thermal mass corrections come from the scalar loops, from the neutral Goldstone loop, and from the gauge boson loop as shown in Fig. 10.

The scalar loop contribution from χ^4 term is given by

$$\text{scalar loop from} \chi^4 = 3\lambda_h i \int \frac{d^4k}{(2\pi)^4} \frac{1}{k^2} \to 3\lambda_h T\sum_n \int \frac{d^3\mathbf{k}}{(2\pi)^3} \frac{1}{\omega_n^2 + |\mathbf{k}|^2} = \frac{\lambda_h}{4} T^2. \tag{A6}$$
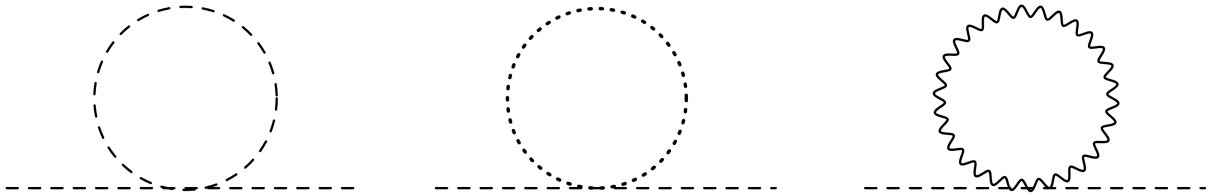

FIG. 10.   Left: thermal mass correction to the scalar field χ complex scalar loop exchange indicated by the dashed line. Middle: same as the left figure except that the thermal loop correction is from the Goldstone loop (small dashed line). Right: same as the left figures except that the thermal loop correction is from the $U(1)$ gauge field loop (wavy line).

The prefactors can be understood as the following: The contraction of $\langle \chi(x)|\frac{\lambda_h}{4}\chi\chi\chi\chi(z)|\chi(y)\rangle$ has in total 4×3 ways and gives rise to a factor 3λ, and the additional I in the front is from the computation of the amplitudes, i.e., $i\mathcal{M}$. The scalar loop contribution from $\chi^2(G_h^0)^2$ term is given by

$$\text{Goldstone loop from } \chi^2(G_h^0)^2 = \lambda_h i \int \frac{\mathrm{d}^4 k}{(2\pi)^4}\frac{1}{k^2} \rightarrow \lambda_h T \sum_n \int \frac{\mathrm{d}^3 \mathbf{k}}{(2\pi)^3}\frac{1}{\omega_n^2 + |\mathbf{k}|^2} = \frac{\lambda_h}{12}T^2, \tag{A7}$$

where the contraction of $\langle \chi(x)|\frac{\lambda_h}{2}\chi\chi(z)G_h^0 G_h^0(z)|\chi(y)\rangle$ has two ways and thus gives rise to a factor $2 \times (-i\frac{\lambda_h}{2}) = -i\lambda_h$. Thus, the total scalar thermal contribution is the sum of the two above results,

$$\text{scalar and Goldstone loops} = \frac{\lambda_h}{4}T^2 + \frac{\lambda_h}{12}T^2 = \frac{\lambda_h}{3}T^2, \tag{A8}$$

which is different from the SM Higgs thermal mass $\frac{\lambda}{2}T^2$, owing to the fact that there are also contributions from the two charged Goldstone bosons. The gauge boson loop contributions to the scalar mass is given by

$$\text{Gauge boson loop} = i(ig_x^2) \int \frac{\mathrm{d}^4 k}{(2\pi)^4}\text{Tr}[\Delta_{\mu\nu}(k)] \rightarrow 3g_x^2 T \sum_n \int \frac{\mathrm{d}^3 \mathbf{k}}{(2\pi)^3}\frac{1}{\omega_n^2 + |\mathbf{k}|^2} = \frac{g_x^2}{4}T^2, \tag{A9}$$

where $\Delta_{\mu\nu}(k)$ is the gauge boson propagator in the Landau gauge given by $\Delta_{\mu\nu}(k) = \frac{-i}{k^2}(g^{\mu\nu} - \frac{k^\mu k^\nu}{k^2})$. The contraction of $\langle \chi(x)|\frac{1}{2}gx^2\chi\chi(z)AA(z)|\chi(y)\rangle$ gives rise to a total front factor $2 \times (i\frac{1}{2}g_x^2) = ig_x^2$.

Thus, in this case the total thermal mass for the dark scalar field $\Pi_\chi(T)$ is given by

$$\Pi_\chi = \frac{1}{3}\lambda_h T^2 + \frac{1}{4}g_x^2 T^2. \tag{A10}$$

2. Thermal mass for the $U(1)$ gauge boson

Next we compute the thermal mass for the longitudinal contribution to the $U(1)$ gauge boson mass γ'. Here the polarization tensors of vector bosons can split into components of longitudinal (L) and transverse (T) polarization so that

$$\Pi^{\mu\nu} = \Pi^T T^{\mu\nu} + \Pi^L L^{\mu\nu} \tag{A11}$$

with projection operators $T^{\mu\nu} = \text{diag}\{0, 2, 2, 2\}$ and $L^{\mu\nu} = \text{diag}\{-1, 0, 0, 0\}$ in the IR limit [127]. The gauge boson thermal mass corrections come from scalar and fermion

contributions: In this case the thermal mass corrections to the γ' mass come from scalar and fermion loop contributions as shown in Fig. 11. The calculation of the scalar loop contribution is easier to be performed considering the complex $U(1)_X$ field Φ which has 2 degrees of freedom and it represented by the double dashed line in Fig. 11. The corresponding Lagrangian reads

$$\mathcal{L} \supset |D_\mu \Phi|^2 \rightarrow g_x^2 A^2 \Phi\Phi^* + ig_x A_\mu(\Phi^*\partial^\mu\Phi - \Phi\partial^\mu\Phi^*), \tag{A12}$$

which gives $i2g_x^2$ for the four-point vertex $AA\Phi\Phi^*$ and $-2g_x k^\mu$ for the three-point vertex $A^\mu\Phi\Phi^*$. The scalar loop contribution is

scalar loop

$$= 2 \times \frac{i}{2} \int \frac{\mathrm{d}^4 k}{(2\pi)^4}\left[(i2g_x^2 g^{\mu\nu})\frac{i}{k^2} + \frac{(2gk^\mu)(-2g_x k^\nu)(i)^2}{(k^2)^2}\right], \tag{A13}$$

where the prefactor 2 is from Φ being a complex scalar, and $1/2$ is the symmetric factor due to the two external gauge
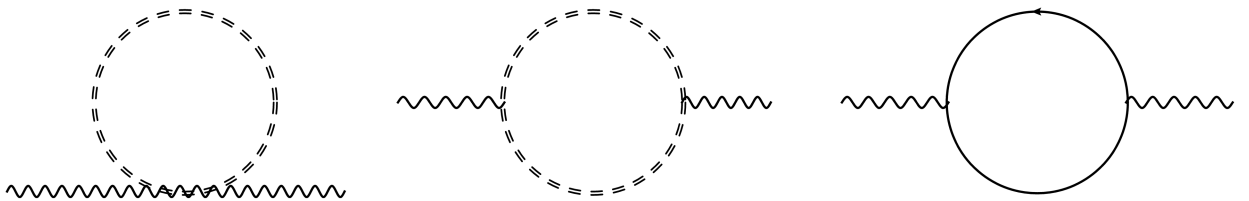

FIG. 11. Thermal mass corrections to the gauge boson mass from the complex scalar loop with a four point vertex (left) and with a three point vertex (middle), and from the Dirac fermion loop (right).

boson legs. One still needs to multiply the 2 from the complex Φ. For the nonzero contribution to the longitudinal part we get

$$\Pi^L = -\Pi^{00} = i2g_x^2 \int \frac{d^4k}{(2\pi)^4} \left[\frac{1}{k^2} - \frac{2k_0^2}{(k^2)^2} \right] \to 2g_x^2 T \sum_n \int \frac{d^3\mathbf{k}}{(2\pi)^3} \left[\frac{1}{\omega_n^2 + |\mathbf{k}|^2} - \frac{2\omega_n^2}{(\omega_n^2 + |\mathbf{k}|^2)^2} \right]$$

$$= \frac{g_x^2}{3} T^2. \tag{A14}$$

The $U(1)_X$ charged fermion loop contribution given by the right diagram in Fig. 11 is given by

$$\text{fermion loop} = (-)i \int \frac{d^4k}{(2\pi)^4} (ig_x)^2 \frac{(i)^2 \text{Tr}(\gamma^\mu \not{k} \gamma^\nu \not{k})}{(k^2)^2} = -i4g_x^2 \int \frac{d^4k}{(2\pi)^4} \frac{2k^\mu k^\nu - k^2 g^{\mu\nu}}{(k^2)^2}, \tag{A15}$$

which gives contribution to Π_L so that

$$\Pi^L = -\Pi^{00} = i4g_x^2 \int \frac{d^4k}{(2\pi)^4} \frac{k_0^2 + |\mathbf{k}|^2}{(k^2)^2} \to -4g_x^2 T \sum_n \int \frac{d^3\mathbf{k}}{(2\pi)^3} \frac{\omega_n^2 + |\mathbf{k}|^2}{(\omega_n^2 + |\mathbf{k}|^2)^2} = \frac{g_x^2}{3} T^2. \tag{A16}$$

This is the contribution from a Dirac fermion exchange. For a chiral fermion exchange, either left- or right-handed, the contribution to the thermal mass is $\frac{g_x^2}{6} T^2$. For an Abelian gauge theory there is no gauge boson loop contribution.

From the above analysis we deduce that, if in addition to the complex scalar field Φ, there are n numbers of dark *chiral* fermion X_i (either left- or right-handed) with the $U(1)_X$ charge Q_i, then the thermal mass for the dark sector gauge boson γ' is given by

$$\Pi_{\gamma'} = \frac{1}{3} g_x^2 T^2 + \sum_{i=1}^n \frac{1}{6} g_x^2 Q_i^2 T^2, \tag{A17}$$

where the first term on the right-hand side arises from a complex scalar loop and the second term from N chiral fermion loops.

3. Daisy resummation

As discussed in a number of works in temperature-dependent perturbation theory, the summation over higher loops can produce the same size correction as the one loop and should be taken into account [44,127–129]. Thus, one finds that at the nth order, the n-loop daisy diagram with $n-1$ petals (see Fig. 12), also called the ring diagram, gives the dominant contribution. The daisy diagrams can be resumed by adding up propagators with increasing number of attached loops. Each loop can contribute a thermal mass correction $\Pi(T_h) = \Pi_1(T_h)$, where $\Pi_1(T_h)$ is the one-loop thermal mass correction, derived above. The sum of all the propagators can be written as

$$\frac{1}{p^2 - m^2} + \frac{\Pi(T_h)}{(p^2 - m^2)^2} + \frac{\Pi^2(T_h)}{(p^2 - m^2)^3} + \cdots$$

$$= \frac{1}{p^2 - m^2 - \Pi(T_h)},$$

which is equivalent to adding a thermal contribution to the mass in the propagator, i.e.,

$$m^2(\chi_c) \to m^2(\chi_c) + \Pi(T_h). \tag{A18}$$

Now the one-loop contribution at zero temperature is given by

$$V_{1h}^{(0)}(\chi_c) = \sum_i \frac{N_i}{2} \int \frac{d^4k_E}{(2\pi)^4} \ln[k_E^2 + m_i^2(\chi_c)], \tag{A19}$$

where i runs over all the particles that enter the loop and N_i are the degrees of freedom for particle i. The regularized and renormalized one-loop potential as given by the right-hand side under the $\overline{\text{MS}}$ scheme is the familiar Coleman-Weinberg potential. From here on we follow the procedure
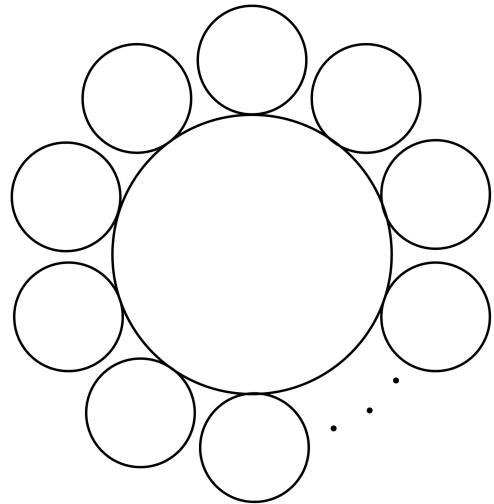

FIG. 12. A daisy or ring diagram which contributes to thermal potential.

in the preceding analysis and using the imaginary time formalism we replace the integral over k_E^0 by a summation over the Matsubara frequencies as given by Eq. (A1), where ω_n^{b} are for bosons and ω_n^{f} are for fermions and $\Delta V_{1h}^{T_h}(\chi_c, T_h))$ at finite temperature is given by

$$\Delta V_{1h}^{T_h}(\chi_c, T_h) = \sum_i \frac{N_i T_h}{2} \sum_{n=-\infty}^{+\infty} \int \frac{\mathrm{d}^3 \mathbf{k}}{(2\pi)^3} \ln[\mathbf{k}^2 + \omega_n^2 + m_i^2(\chi_c)]. \tag{A20}$$

After the replacement Eq. (A18), the thermal one-loop potential $\Delta V_{1h}^{(T_h)}(\chi_c, T_h)$ reads

$$\Delta V_{1h}^{(T_h)}(\chi_c, T_h) \to \sum_i \frac{N_i T_h}{2} \left\{ \sum_{n\neq 0} \int \frac{\mathrm{d}^3 \mathbf{k}}{(2\pi)^3} \ln[\mathbf{k}^2 + \omega_n^2 + m_i^2(\chi_c)] + \int \frac{\mathrm{d}^3 \mathbf{k}}{(2\pi)^3} \ln[\mathbf{k}^2 + m_i^2(\chi_c) + \Pi(T_h)] \right\}$$

$$= \sum_i \frac{N_i T_h}{2} \left\{ \sum_{n\neq 0} \int \frac{\mathrm{d}^3 \mathbf{k}}{(2\pi)^3} \ln[\mathbf{k}^2 + \omega_n^2 + m_i^2(\chi_c)] + \int \frac{\mathrm{d}^3 \mathbf{k}}{(2\pi)^3} \ln[\mathbf{k}^2 + m_i^2(\chi_c)] \right.$$

$$\left. + \int \frac{\mathrm{d}^3 \mathbf{k}}{(2\pi)^3} \ln\left[1 + \frac{\Pi(T_h)}{\mathbf{k}^2 + m_i^2(\chi_c)}\right] \right\}$$

$$= \sum_i \frac{N_i T_h}{2} \sum_{n=-\infty}^{+\infty} \int \frac{\mathrm{d}^3 \mathbf{k}}{(2\pi)^3} \ln[\mathbf{k}^2 + \omega_n^2 + m_i^2(\chi_c)] + \sum_i \frac{\bar{N}_i T_h}{2} \int \frac{\mathrm{d}^3 \mathbf{k}}{(2\pi)^3} \ln\left[1 + \frac{\Pi(T_h)}{\mathbf{k}^2 + m_i^2(\chi_c)}\right]$$

$$= \Delta V_{1h}^{(T_h)}(\chi_c, T_h) + V_h^{\mathrm{daisy}}(\chi_c, T_h),$$

where $\bar{N}_i$ are the bosonic degrees of freedom which incur the mass shift. The daisy diagram contribution to the effective potential from one particle is computed to be

$$V_h^{\mathrm{daisy}}(\chi_c, T_h) = \frac{T_h}{2} \int \frac{\mathrm{d}^3 \mathbf{k}}{(2\pi)^3} \ln\left[1 + \frac{\Pi(T_h)}{\mathbf{k}^2 + m^2(\chi_c)}\right] = \lim_{\Lambda\to+\infty} \frac{T_h}{4\pi^2} \int_0^\Lambda \mathrm{d}k k^2 \ln\left[1 + \frac{\Pi(T_h)}{\mathbf{k}^2 + m^2(\chi_c)}\right]$$

$$= \lim_{\Lambda\to+\infty} \frac{T_h}{4\pi^2} \times \frac{1}{3} \left\{ 2\Lambda\Pi(T_h) + \Lambda^3 \ln\left[1 + \frac{\Pi(T_h)}{m^2(\chi_c) + \Lambda^2}\right] + 2m^3(\chi_c)\tan^{-1}\left(\frac{\Lambda}{m}\right) \right.$$

$$\left. - 2[m^2(\chi_c) + \Pi(T_h)]^{3/2}\tan^{-1}\left[\frac{\Lambda}{\sqrt{m^2(\chi_c) + \Pi(T_h)}}\right] \right\}$$

$$\to -\frac{T_h}{12\pi} \{[m^2(\chi_c) + \Pi(T_h)]^{3/2} - m^3(\chi_c)\}, \tag{A21}$$

where on the last line we drop the divergent pieces which are canceled by counterterms, and $\tan^{-1}(\frac{\Lambda}{m_\times}) \to \frac{\pi}{2}$ when taking $\Lambda \to +\infty$ where $m_\times$ is a mass taken positive.

APPENDIX B: EFFECTIVE THERMAL POTENTIAL OF THE VISIBLE SECTOR

The effective Higgs potential in the standard model, including the temperature-dependent part, is well known. It is given by the sum of the zero temperature tree and zero temperature Coleman-Weinberg one-loop potential [130], temperature-dependent one-loop correction, and "daisy diagrams" [44,45,49,128,129,131–133]. We give a brief discussion of it here for completeness. Thus, consider the tree level potential for the standard model with the complex Higgs doublet field H so that

$$V(H, H^\dagger) = -\mu^2 H^\dagger H + \lambda (H^\dagger H)^2. \tag{B1}$$

We write the doublet of the Higgs field H so that

$$H = \begin{pmatrix} G^+ \\ \frac{(\phi_c + \phi + iG_3)}{\sqrt{2}} \end{pmatrix}, \tag{B2}$$

where ϕ_c is the background fields, ϕ is the Higgs field, and $G^+ = (G_1 + iG_2)/\sqrt{2}$ where $G_{1,2,3}$ are the three Goldstone bosons. The tree level potential is given by

$$V_0(\phi_c) = -\frac{\mu^2}{2} \phi_c^2 + \frac{\lambda}{4} \phi_c^4. \tag{B3}$$

To one-loop order, the effective potential of the standard model including temperature-dependent contributions is given by

$$V_{\mathrm{eff}}(\phi_c, T) = V_0(\phi_c) + V_1^{(0)}(\phi_c) + \Delta V_1^{(T)}(\phi_c, T) + V^{\mathrm{daisy}}(\phi_c, T) + \delta V^{(T)}(\phi_c, T), \tag{B4}$$

where $V_1^{0)}$ is the zero temperature one-loop potential, $\Delta V_1^{(T)}$ is the temperature-dependent one-loop contribution, V^{daisy} is the daisy loop contribution, and $\delta V^{(T)}$ are the counterterms to remove divergent terms. Thus, $V_1^{(0)}(\phi_c)$ is given by

$$V_1^{(0)}(\phi_c) = \sum_i \frac{N_i(-1)^{2s_i}}{64\pi^2} m_i^4(\phi_c)\left[\ln\left(\frac{m_i^2(\phi_c)}{\Lambda^2}\right) - \mathcal{C}_i\right],$$
(B5)

where the sum i runs over all particles in the theory with N_i degrees of freedom for particle i with mass $m_i(\phi_c)$ and spin s_i, Λ is the renormalization scale, and $\mathcal{C}_i$ equals 5/6 for gauge bosons and 3/2 for fermions and scalars in $\overline{\text{MS}}$ renormalization. The relevant contribution arises from the gauge bosons Z and $W^\pm$, the top quark, the Higgs boson, and the Goldstone bosons. Thus, for the SM i runs through $\{Z, W, t, H, G_3, G^\pm\}$ and the corresponding front factors are $N_i = \{3, 6, 12, 1, 1, 1, 1\}$. The field-dependent masses $m_i^2(\phi_c)$ are given by

$$m_h^2(\phi_c) = -\mu^2 + 3\lambda\phi_c^2, \qquad m_t^2(\phi_c) = \frac{1}{2}y_t^2\phi_c^2, \quad \text{(B6)}$$

$$m_W^2(\phi_c) = \frac{1}{4}g_2^2\phi_c^2, \qquad M_Z^2(\phi_c) = \frac{1}{4}(g_2^2 + g_Y^2)\phi_c^2, \quad \text{(B7)}$$

$$m_{G_3} = m_{G^\pm} = -\mu^2 + \lambda\phi_c^2. \quad \text{(B8)}$$

The thermal correction in one-loop order arise from bosons and fermions which couple to the Higgs field and is given by

$$\Delta V_1^{(T)}(\phi, T) = \frac{T^4}{2\pi^2}\left[6J_B\left(\frac{m_W}{T}\right) + 3J_B\left(\frac{m_Z}{T}\right) + J_B\left(\frac{m_h}{T}\right)\right.$$
$$\left. + 3J_B\left(\frac{m_G}{T}\right) - 12J_F\left(\frac{m_t}{T}\right)\right],$$
(B9)

where the functions J_B and J_F are defined as in Eq. (2.8). Further, as noted earlier one needs to include the daisy resummation contribution to the potential, which in this case is given by

$$V_1^{\text{daisy}}(\phi, T)$$
$$= \frac{T}{12\pi}\sum_{B'=Z,W,H} g_{B'}\{m_{B'}^3(\phi) - [m_{B'}^2(\phi) + \Pi_{B'}(T)]^{3/2}\},$$
(B10)

where the sum runs only over scalars and longitudinal vectors. Here $g_{B'} = \{1, 2, 1\}$ for $B' = \{Z, W, H\}$, and there

are no contributions to the transverse modes and to the fermion masses. Thus, the thermal contributions to the masses $\Pi_{B'}(T)$ are given by [127]

$$\Pi_H(T) = \left[\frac{1}{6}(3g_2^2 + g_Y^2) + \frac{1}{4}y_t^2 + \frac{1}{2}\lambda\right]T^2, \quad \text{(B11)}$$

$$\Pi_W(T) = \Pi_Z(T) = \frac{11}{6}g_2^2T^2, \quad \text{(B12)}$$

at the leading order in T^2 where y_t is defined so that $m_t = \frac{1}{\sqrt{2}}y_t v$ and $v \simeq 246$ GeV.

APPENDIX C: FURTHER DETAILS OF VISIBLE AND HIDDEN SECTOR INTERACTIONS

As noted in Sec. II the analysis of synchronous evolution is very general and applicable to a wide array of portals connecting the hidden and the visible sectors. In this work for the specific hidden sector with a $U(1)$ gauge invariance broken by the Higgs mechanism, we used the kinetic mixing between the hidden and the visible sectors as noted in Sec. II B. Here one includes a mixing term $-\frac{\delta}{2}A^{\mu\nu}B_{\mu\nu}$ in the Lagrangian, where $A^{\mu\nu}$ is the field strength of the hidden sector $U(1)$ field A^μ and $B_{\mu\nu}$ is the field strength of the $U(1)_Y$ hypercharge field B_μ of the visible sector. Since the standard model is based on the group $SU(2) \times U(1)_Y$ we will have a coupling of three gauge fields A_3^μ, B^μ, A^μ, where A_3^μ is the third component of the $SU(2)_L$ gauge field A_a^μ ($a = 1, 2, 3$) of the standard model. After electroweak symmetry breaking and in the canonical basis where the kinetic energies of the gauge fields are diagonalized and normalized, the physical fields are $Z^\mu, A_\gamma^\mu, A_{\gamma'}^\mu$, where Z is the Z boson of the standard model, A_γ is the photon, and $A_{\gamma'}$ is the dark photon. Thus, the couplings governing the dark sector and the feeble interactions of the dark sector with the visible sector are given by

$$\Delta\mathcal{L}^{\text{int}} = \bar{D}\gamma^\mu(g_{\gamma'}A_\mu^{\gamma'} + g_Z Z_\mu + g_\gamma A_\mu^\gamma)D$$
$$+ \frac{g_2}{2\cos\theta}\bar{\psi}_f\gamma^\mu[(v_f' - \gamma_5 a_f')A_\mu^{\gamma'}]\psi_f - \Delta V_h, \Delta V_h$$
$$= \frac{1}{2}m_\chi^2\chi^2 + \frac{1}{2}m_{\gamma'}^2 A_\mu^{\gamma'}A^{\gamma'\mu} + g_x^2 v_h\chi A_\mu^{\gamma'}A^{\gamma'\mu}$$
$$+ \frac{1}{2}g_x^2\chi^2 A_\mu^{\gamma'}A^{\gamma'\mu}, \quad \text{(C1)}$$

$$v_f' = -\cos\psi[(\tan\psi - s_\delta\sin\theta)T_{3f}$$
$$- 2\sin^2\theta(-s_\delta\csc\theta + \tan\psi)Q_f], \quad \text{(C2)}$$

$$a_f' = -\cos\psi(\tan\psi - s_\delta\sin\theta)T_{3f}. \quad \text{(C3)}$$

Here $s_\delta = \sinh \delta$ and $c_\delta = \cosh \delta$, and f runs over all SM fermions, $m_{\gamma'} = g_x v_h$ and $m_\chi = \sqrt{2\lambda_h} v_h$. Further, T_{3f} is the third component of isospin, and Q_f is the electric charge for the fermion. The couplings g_Z, g_γ, and $g_{\gamma'}$ that appear above are given by

$$
\begin{aligned}
g_{\gamma'} &= g_X Q_X(\mathcal{R}_{11} - s_\delta \mathcal{R}_{21}), \\
g_\gamma &= g_X Q_X(\mathcal{R}_{13} - s_\delta \mathcal{R}_{23}), \\
g_Z &= g_X Q_X(\mathcal{R}_{12} - s_\delta \mathcal{R}_{22}).
\end{aligned}
\tag{C4}
$$

Here the matrix $\mathcal{R}$ is given by Eq. (23) of [58] and it involves three Euler angles (θ, ϕ, ψ) which are given by

$$
\tan\phi = -s_\delta, \qquad \tan\theta = \frac{g_Y}{g_2} c_\delta \cos\phi,
$$

$$
\tan 2\psi = \frac{2\bar{\delta}m_Z^2 \sin\theta}{m_{\gamma'}^2 - m_Z^2 + (m_{\gamma'}^2 + m_Z^2 - m_W^2)\bar{\delta}^2},
\tag{C5}
$$

where $\bar{\delta} = -\delta/\sqrt{1-\delta^2}$. In addition to the above, there is also a modification of the standard model couplings. Thus, in the canonically diagonalized basis the couplings of Z_μ and A_μ^γ are given by [58,63]

$$
\Delta\mathcal{L}'_{\text{SM}} = \frac{g_2}{2\cos\theta}\bar{\psi}_f\gamma^\mu[(v_f - \gamma_5 a_f)Z_\mu]\psi_f + e\bar{\psi}_f\gamma^\mu Q_f A_\mu^\gamma \psi_f.
\tag{C6}
$$

Modifications to the visible sector interactions appear in the vector and axial vector couplings so that (see [60,61,65,134])

$$
\begin{aligned}
v_f &= \cos\psi[(1 + s_\delta \tan\psi \sin\theta)T_{3f} \\
&\quad - 2\sin^2\theta(1 + s_\delta \csc\theta \tan\psi)Q_f], \\
a_f &= \cos\psi(1 + s_\delta \tan\psi \sin\theta)T_{3f}.
\end{aligned}
\tag{C7}
$$

APPENDIX D: SCATTERING CROSS SECTIONS FOR $\xi(T)$ AND YIELD EQUATIONS FOR THE HIDDEN SECTOR FIELDS

The analysis of yields in Eqs. (2.21)–(2.23) requires several cross sections. The cross sections $\sigma_{D\bar{D}\to\gamma'\gamma'}$, $\sigma_{D\bar{D}\to i\bar{i}}$, $\sigma_{i\bar{i}\to\gamma'\gamma'}$, and $\Gamma_{\gamma'\to i\bar{i}}$ are given in [47,61]. The additional cross section needed is $\sigma_{\chi\chi\to\gamma'\gamma'}$. The Feynman diagrams for it are in Fig. 13. This cross section is given by

$$
\begin{aligned}
\sigma^{\chi\chi\to\gamma'\gamma'}(s, T_h) = {}&\frac{g_x^4(12m_{\gamma'}^4 - 4m_{\gamma'}^2 s + s^2)}{512\pi m_{\gamma'} s^2}\left(\frac{\sqrt{(s-4m_\chi^2)(s-4m_{\gamma'}^2)}}{(m_\chi^2 - s)^2(m_\chi^4 - 4m\chi^2 m_{\gamma'}^2 + m_{\gamma'}^2 s)}(8g_x^4 v_h^4(m_\chi^2 - s)^2\right. \\
&+ (m_\chi^2 - s)^2(m_\chi^4 - m_\chi^2 m_{\gamma'}^2 + m_{\gamma'}^2 s)) + \frac{8g_x^2 v_h^2}{2m_\chi^4 - 3m_\chi^2 s + s^2}\left.(\log A(m_\chi^2(2v_h^2 g_x^2 - 3s) + s(2v_h^2 g_x^2 + s) + 2m_\chi^4))\right),
\end{aligned}
\tag{D1}
$$

$$
A = \frac{\sqrt{(s-4m_\chi^2)(s-m_{\gamma'}^2)} - 2m_\chi^2 + s}{-\sqrt{(s-4m_\chi^2)(s-m_{\gamma'}^2)} - 2m_\chi^2 + s},
\tag{D2}
$$

where s is the Mandelstam variable. The cross section for the reverse process is then given by

$$
2\sqrt{s-4m_\chi^2}\,\sigma^{\chi\chi\to\gamma'\gamma'}(s, T_h) = 9\sqrt{s-4m_{\gamma'}^2}\,\sigma^{\gamma'\gamma'\to\chi\chi}(s, T_h).
\tag{D3}
$$
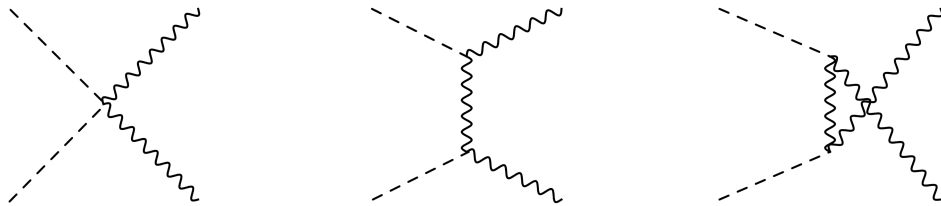

FIG. 13.   The Feynman diagram for the annihilation process $\chi\chi \to \gamma'\gamma'$.

Additionally, we also need the decay width for the process $\chi \to \gamma'\gamma'$. This is given by

$$\Gamma_{\chi \to \gamma'\gamma'}(s) = \frac{g_x^4 v_h^2}{128\pi m_\chi m_{\gamma'}^4} \sqrt{1 - \frac{4m_{\gamma'}^2}{m_\chi^2}} (-4m_\chi^2 m_{\gamma'}^2 + m_\chi^4 + 12m_{\gamma'}^4). \tag{D4}$$

We also define here j_h that enters Eq. (2.20),

$$j_h = \sum_i [2Y_i^{\text{eq}}(T)^2 J(i\bar{i} \to D\bar{D})(T) + Y_i^{\text{eq}}(T)^2 J(i\bar{i} \to \gamma')(T)]\mathbb{s}^2 - Y_{\gamma'} J(\gamma' \to i\bar{i})(T_h)\mathbb{s}, \tag{D5}$$

$$Y_i^{\text{eq}} = \frac{n_i^{\text{eq}}}{\mathbb{s}} = \frac{g_i}{2\pi^2 \mathbb{s}} m_i^2 T K_2(m_i/T), \tag{D6}$$

where K_2 is the modified Bessel function of the second kind and degree two. Further, g_i is the number of degrees of freedom of particle i and mass m_i and the source functions J are defined so that The J functions that appear in Eq. (D5) are defined as

$$n_i^{\text{eq}}(T)^2 J(i\bar{i} \to D\bar{D})(T) = \frac{T}{32\pi^4} \int_{s_0}^{\infty} ds \sigma_{D\bar{D} \to i\bar{i}} s(s - s_0) K_2(\sqrt{s}/T), \tag{D7}$$

$$n_i^{\text{eq}}(T)^2 J(i\bar{i} \to \gamma')(T) = \frac{T}{32\pi^4} \int_{s_0}^{\infty} ds \sigma_{i\bar{i} \to \gamma'} s(s - s_0) K_2(\sqrt{s}/T), \tag{D8}$$

$$n_{\gamma'} J(\gamma' \to i\bar{i})(T_h) = n_{\gamma'} m_{\gamma'} \Gamma_{\gamma' \to i\bar{i}}, \tag{D9}$$

$$n_i^{\text{eq}}(T)^2 \langle \sigma v \rangle_{i\bar{i} \to \gamma'}(T) = \frac{T}{32\pi^4} \int_{s_0}^{\infty} ds \sigma(s) \sqrt{s}(s - s_0) K_1(\sqrt{s}/T), \tag{D10}$$

where K_1 is the modified Bessel function of the second kind and degree one and s_0 is the minimum of the Mandelstam variable s. We note that there are additional contributions one can include in the analysis, i.e., $i\bar{i} \to \gamma'\gamma, \gamma'Z, \gamma'\gamma'$. Their contributions are relatively small compared to $i\bar{i} \to \gamma'$ and are neglected.

APPENDIX E: ENERGY AND PRESSURE DENSITIES AWAY FROM EQUILIBRIUM

If one assumes that the hidden sector was in thermal equilibrium at all times, then the particle distributions will follow the Fermi-Dirac or Bose-Einstein statistics as appropriate. In this case, the energy density ρ_h and the pressure density p_h in the hidden sector are given by [135,136]

$$\rho_h = \sum_i \rho_i = \sum_i \frac{g_i T_h^4}{2\pi^2} \int_{x_i}^{\infty} \frac{\sqrt{x^2 - x_i^2}}{e^x \pm 1} x^2 dx, i \in \{\gamma', D, \chi\},$$

$$p_h = \sum_i p_i = \sum_i \frac{g_i T_h^3}{6\pi^2} \int_{x_i}^{\infty} \frac{(x^2 - x_i^2)^{\frac{3}{2}}}{e^x \pm 1} dx, i \in \{\gamma', D, \chi\},$$

$$\tag{E1}$$

where $g_{\gamma'} = 3$, $g_D = 4$, $g_\chi = 3$, $x_i = \frac{m_i}{T_h}$ and plus is for fermions, while minus is for bosons. If a massive particle remained in thermal equilibrium until today, its energy density, $\rho_i \sim (m_i/T)^{3/2} \exp(-m_i/T)$, would be negligible because of the exponential factor. However, as pointed out in [137] if the interactions of the particles freeze out before complete annihilation, the particles may have a significant relic abundance today. Often in the discussion of freeze-out, it is generally assumed that $\rho = \rho_{\text{eq}}$ where ρ_{eq} refers to the equilibrium density. However, the more precise way to compute the energy density in a freeze-out situation is to take

$$\rho_h = \rho_{h,\text{eq}} + \rho_{h,\text{relic}}. \tag{E2}$$

As suggested in [137], $\rho_{h,\text{relic}}$ could be computed using the yield equation to obtain the number density

$$Y_{h,\text{relic}} = \frac{n_{h,\text{relic}}}{\mathbb{s}} \Rightarrow n_{h,\text{relic}} = Y_{h,\text{relic}} \mathbb{s}, \tag{E3}$$

which allows a computation of the number density $n_{h,\text{relic}}$ from where we can compute the $g_{n,\text{relic}}^h$ so that

$$n_{h,\text{relic}} = \frac{\zeta(3)}{\pi^2} g_{n,\text{relic}}^h T_h^3. \tag{E4}$$

Next we set the effective energy degrees of freedom from the relic density so that

$$g^h_{\rho,\text{relic}} = g^h_{n,\text{relic}} \qquad (E5)$$

and use the relation

$$\rho_{h,\text{relic}} = \frac{\pi^2}{30} g^h_{\rho,\text{relic}} T^4_h \qquad (E6)$$

to find $\rho_{h,\text{relic}}$ and ρ_h. In most cases, this analysis is not necessary since $\rho_{h,\text{relic}} \ll \rho_{h,\text{eq}}$. However, such an analysis becomes relevant when we are dealing with the decoupling of the entire hidden sector since in this situation we have $\rho_{h,\text{relic}} \gg \rho_{h,\text{eq}}$. A similar analysis holds for the pressure density p_h. Aside from the correction to the density discussed above, the density of the hidden sector should freeze out when the two sectors are fully decoupled. This analysis will be similar to the analysis in cannibalism dark matter [138]. For the current model, the decoupling happens when (i) all interactions between the hidden sector and the visible sector decouple and (ii) the dark photon decays out.

[1] B. P. Abbott *et al.* (LIGO Scientific and Virgo Collaborations), Phys. Rev. Lett. **116**, 061102 (2016).
[2] D. A. Kirzhnits, JETP Lett. **15**, 529 (1972).
[3] D. A. Kirzhnits and A. D. Linde, Phys. Lett. **42B**, 471 (1972).
[4] E. Witten, Nucl. Phys. **B177**, 477 (1981).
[5] A. H. Guth and E. J. Weinberg, Phys. Rev. D **23**, 876 (1981).
[6] P. J. Steinhardt, Phys. Rev. D **25**, 2074 (1982).
[7] E. Witten, Phys. Rev. D **30**, 272 (1984).
[8] C. J. Hogan, Mon. Not. R. Astron. Soc. **218**, 629 (1986).
[9] M. Kamionkowski, A. Kosowsky, and M. S. Turner, Phys. Rev. D **49**, 2837 (1994).
[10] S. Y. Khlebnikov and I. I. Tkachev, Phys. Rev. D **56**, 653 (1997).
[11] R. Easther, J. T. Giblin, Jr., and E. A. Lim, Phys. Rev. Lett. **99**, 221301 (2007).
[12] J. Garcia-Bellido, D. G. Figueroa, and A. Sastre, Phys. Rev. D **77**, 043517 (2008).
[13] A. G. Cohen, D. B. Kaplan, and A. E. Nelson, Phys. Lett. B **245**, 561 (1990).
[14] M. Carena, J. M. Moreno, M. Quiros, M. Seco, and C. E. M. Wagner, Nucl. Phys. **B599**, 158 (2001).
[15] J. M. Cline, arXiv:hep-ph/0609145.
[16] G. A. White, *A Pedagogical Introduction to Electroweak Baryogenesis* (Morgan & Claypool, 2016), ISBN 978-1-68174-456-8, 978-1-68174-457-5.
[17] J. M. Cline, Proc. Sci. TASI2018 (**2019**) 001 [arXiv:1807.08749].
[18] L. Dolan and R. Jackiw, Phys. Rev. D **9**, 3320 (1974).
[19] S. Weinberg, Phys. Rev. D **9**, 3357 (1974).
[20] F. C. Adams, Phys. Rev. D **48**, 2800 (1993).
[21] R. R. Parwani, Phys. Rev. D **45**, 4695 (1992); **48**, 5965(E) (1993).
[22] P. B. Arnold and O. Espinosa, Phys. Rev. D **47**, 3546 (1993); **50**, 6662(E) (1994).
[23] J. R. Espinosa, M. Quiros, and F. Zwirner, Phys. Lett. B **314**, 206 (1993).
[24] M. Quiros, arXiv:hep-ph/9304284.
[25] D. Curtin, P. Meade, and H. Ramani, Eur. Phys. J. C **78**, 787 (2018).
[26] J. R. Espinosa and M. Quiros, Phys. Rev. D **76**, 076004 (2007).
[27] J. R. Espinosa, T. Konstandin, J. M. No, and M. Quiros, Phys. Rev. D **78**, 123528 (2008).
[28] D. Azevedo, P. M. Ferreira, M. M. Muhlleitner, S. Patel, R. Santos, and J. Wittbrodt, J. High Energy Phys. 11 (2018) 091.
[29] A. Mohamadnejad, J. High Energy Phys. 03 (2022) 188.
[30] L. Biermann, M. Mühlleitner, and J. Müller, Eur. Phys. J. C **83**, 439 (2023).
[31] W. Wang, W. L. Xu, and J. M. Yang, Eur. Phys. J. Plus **138**, 781 (2023).
[32] T. Bringmann, T. E. Gonzalo, F. Kahlhoefer, J. Matuszak, and C. Tasillo, J. Cosmol. Astropart. Phys. 05 (2024) 065.
[33] A. Addazi, Mod. Phys. Lett. A **32**, 1750049 (2017).
[34] M. Aoki, H. Goto, and J. Kubo, Phys. Rev. D **96**, 075045 (2017).
[35] R. Pasechnik, M. Reichert, F. Sannino, and Z. W. Wang, J. High Energy Phys. 02 (2024) 159.
[36] P. Schwaller, Phys. Rev. Lett. **115**, 181101 (2015).
[37] A. Addazi and A. Marciano, Chin. Phys. C **42**, 023107 (2018).
[38] M. Fairbairn, E. Hardy, and A. Wickens, J. High Energy Phys. 07 (2019) 044.
[39] R. T. Co, K. Harigaya, and A. Pierce, J. High Energy Phys. 12 (2021) 099.
[40] D. Borah, A. Dasgupta, and S. K. Kang, Phys. Rev. D **104**, 063501 (2021).
[41] T. Abe and K. Hashino, arXiv:2302.13510.
[42] B. Imtiaz, Y. F. Cai, and Y. Wan, Eur. Phys. J. C **79**, 25 (2019).
[43] A. Paul, U. Mukhopadhyay, and D. Majumdar, J. High Energy Phys. 05 (2021) 223.
[44] M. Quiros, arXiv:hep-ph/9901312.
[45] D. E. Morrissey and M. J. Ramsey-Musolf, New J. Phys. **14**, 125003 (2012).
[46] A. Mazumdar and G. White, Rep. Prog. Phys. **82**, 076901 (2019).
[47] J. Li and P. Nath, Phys. Rev. D **108**, 115008 (2023).
[48] P. Nath and J. Li, Lett. High Energy Phys. **2024**, 502 (2024).

[49] M. Sher, Phys. Rep. **179**, 273 (1989).

[50] D. J. Weir, Phil. Trans. R. Soc. A **376**, 20170126 (2018); **381**, 20230212(E) (2023).

[51] P. Athron, C. Balázs, A. Fowlie, L. Morris, and L. Wu, Prog. Part. Nucl. Phys. **135**, 104094 (2024).

[52] M. Breitbach, J. Kopp, E. Madge, T. Opferkuch, and P. Schwaller, J. Cosmol. Astropart. Phys. 07 (2019) 007.

[53] A. Aboubrahim, M. Klasen, and P. Nath, J. Cosmol. Astropart. Phys. 04 (2022) 042.

[54] D. Feldman, B. Kors, and P. Nath, Phys. Rev. D **75**, 023503 (2007).

[55] B. Patt and F. Wilczek, arXiv:hep-ph/0605188.

[56] B. Holdom, Phys. Lett. **166B**, 196 (1986).

[57] B. Kors and P. Nath, Phys. Lett. B **586**, 366 (2004).

[58] D. Feldman, Z. Liu, and P. Nath, Phys. Rev. D **75**, 115001 (2007).

[59] M. Du, Z. Liu, and P. Nath, Phys. Lett. B **834**, 137454 (2022).

[60] A. Aboubrahim, W. Z. Feng, P. Nath, and Z. Y. Wang, Phys. Rev. D **103**, 075014 (2021).

[61] A. Aboubrahim, P. Nath, and Z. Y. Wang, J. High Energy Phys. 12 (2021) 148.

[62] A. Aboubrahim and P. Nath, J. High Energy Phys. 09 (2022) 084.

[63] K. Cheung and T. C. Yuan, J. High Energy Phys. 03 (2007) 120.

[64] B. Kors and P. Nath, Nucl. Phys. **B711**, 112 (2005).

[65] A. Aboubrahim, W. Z. Feng, P. Nath, and Z. Y. Wang, J. High Energy Phys. 06 (2021) 086.

[66] G. Bélanger, F. Boudjema, A. Goudelis, A. Pukhov, and B. Zaldivar, Comput. Phys. Commun. **231**, 173 (2018).

[67] V. Guada, A. Maiezza, and M. Nemevšek, Phys. Rev. D **99**, 056020 (2019).

[68] V. Guada, M. Nemevšek, and M. Pintar, Comput. Phys. Commun. **256**, 107480 (2020).

[69] C. L. Wainwright, Comput. Phys. Commun. **183**, 2006 (2012).

[70] J. R. Espinosa, T. Konstandin, J. M. No, and G. Servant, J. Cosmol. Astropart. Phys. 06 (2010) 028.

[71] S. J. Wang and Z. Y. Yuwen, J. Cosmol. Astropart. Phys. 10 (2022) 047.

[72] L. D. Landau and E. M. Lifshitz, *Fluid Mechanics*, 2nd ed. (Pergamon Press, Oxford, 1989), pp. 85–88, 128–132, 135.

[73] R. Courant and K. O. Friedrichs, *Supersonic Flow and Shock Waves* (Springer-Verlag, Berlin, 1985).

[74] F. Giese, T. Konstandin, K. Schmitz, and J. van de Vis, J. Cosmol. Astropart. Phys. 01 (2021) 072.

[75] F. Giese, T. Konstandin, and J. van de Vis, J. Cosmol. Astropart. Phys. 07 (2020) 057.

[76] J. Kehayias and S. Profumo, J. Cosmol. Astropart. Phys. 03 (2010) 003.

[77] J. Jaeckel, V. V. Khoze, and M. Spannowsky, Phys. Rev. D **94**, 103519 (2016).

[78] A. Katz and A. Riotto, J. Cosmol. Astropart. Phys. 11 (2016) 011.

[79] P. S. B. Dev, F. Ferrer, Y. Zhang, and Y. Zhang, J. Cosmol. Astropart. Phys. 11 (2019) 006.

[80] L. Bian, W. Cheng, H. K. Guo, and Y. Zhang, Chin. Phys. C **45**, 113104 (2021).

[81] J. A. Dror, T. Hiramatsu, K. Kohri, H. Murayama, and G. White, Phys. Rev. Lett. **124**, 041804 (2020).

[82] P. Di Bari, D. Marfatia, and Y. L. Zhou, Phys. Rev. D **102**, 095017 (2020).

[83] X. F. Han, L. Wang, and Y. Zhang, Phys. Rev. D **103**, 035012 (2021).

[84] X. Deng, X. Liu, J. Yang, R. Zhou, and L. Bian, Phys. Rev. D **103**, 055013 (2021).

[85] R. Jinno, B. Shakya, and J. van de Vis, arXiv:2211.06405.

[86] B. Fu, S. F. King, L. Marsili, S. Pascoli, J. Turner, and Y. L. Zhou, Phys. Rev. D **109**, 055025 (2024).

[87] J. Halverson, C. Long, A. Maiti, B. Nelson, and G. Salinas, J. High Energy Phys. 05 (2021) 154.

[88] K. Freese and M. W. Winkler, Phys. Rev. D **107**, 083522 (2023).

[89] S. J. Huber and T. Konstandin, J. Cosmol. Astropart. Phys. 09 (2008) 022.

[90] M. Hindmarsh, S. J. Huber, K. Rummukainen, and D. J. Weir, Phys. Rev. D **92**, 123009 (2015).

[91] C. Caprini, R. Durrer, and G. Servant, J. Cosmol. Astropart. Phys. 12 (2009) 024.

[92] C. Caprini, M. Hindmarsh, S. Huber, T. Konstandin, J. Kozaczuk, G. Nardini, J. M. No, A. Petiteau, P. Schwaller, G. Servant *et al.*, J. Cosmol. Astropart. Phys. 04 (2016) 001.

[93] D. Bodeker and G. D. Moore, J. Cosmol. Astropart. Phys. 05 (2009) 009.

[94] D. Bodeker and G. D. Moore, J. Cosmol. Astropart. Phys. 05 (2017) 025.

[95] W. Y. Ai, B. Garbrecht, and C. Tamarit, J. Cosmol. Astropart. Phys. 03 (2022) 015.

[96] P. Amaro-Seoane *et al.* (LISA Collaboration), arXiv:1702.00786.

[97] J. Baker, J. Bellovary, P. L. Bender, E. Berti, R. Caldwell, J. Camp, J. W. Conklin, N. Cornish, C. Cutler, R. DeRosa *et al.*, arXiv:1907.06482.

[98] P. Amaro-Seoane, S. Aoudia, S. Babak, P. Binetruy, E. Berti, A. Bohe, C. Caprini, M. Colpi, N. J. Cornish, K. Danzmann *et al.*, GW Notes **6**, 4 (2013).

[99] M. Kramer and D. J. Champion, Classical Quantum Gravity **30**, 224009 (2013).

[100] G. Desvignes *et al.* (EPTA Collaboration), Mon. Not. R. Astron. Soc. **458**, 3341 (2016).

[101] G. M. Harry (LIGO Scientific Collaboration), Classical Quantum Gravity **27**, 084006 (2010).

[102] F. Acernese *et al.* (Virgo Collaboration), Classical Quantum Gravity **32**, 024001 (2015).

[103] K. Somiya (KAGRA Collaboration), Classical Quantum Gravity **29**, 124007 (2012).

[104] J. Aasi *et al.* (LIGO Scientific Collaboration), Classical Quantum Gravity **32**, 074001 (2015).

[105] F. Acernese *et al.* (Virgo Collaboration), Classical Quantum Gravity **32**, 024001 (2015).

[106] Y. Hagihara, N. Era, D. Iikawa, and H. Asada, Phys. Rev. D **98**, 064035 (2018).

[107] C. Grojean and G. Servant, Phys. Rev. D **75**, 043507 (2007).

[108] S. Kawamura, T. Nakamura, M. Ando, N. Seto, K. Tsubono, K. Numata, R. Takahashi, S. Nagano, T. Ishikawa, M. Musha *et al.*, Classical Quantum Gravity **23**, S125 (2006).

[109] M. Punturo, M. Abernathy, F. Acernese, B. Allen, N. Andersson, K. Arun, F. Barone, B. Barr, M. Barsuglia, M. Beker *et al.*, Classical Quantum Gravity **27**, 194002 (2010).

[110] B. P. Abbott *et al.* (LIGO Scientific Collaboration), Classical Quantum Gravity **34**, 044001 (2017).

[111] W. H. Ruan, Z. K. Guo, R. G. Cai, and Y. Z. Zhang, Int. J. Mod. Phys. A **35**, 2050075 (2020).

[112] J. Luo *et al.* (TianQin Collaboration), Classical Quantum Gravity **33**, 035010 (2016).

[113] A. Sesana, N. Korsakova, M. A. Sedda, V. Baibhav, E. Barausse, S. Barke, E. Berti, M. Bonetti, P. R. Capelo, C. Caprini *et al.*, Exp. Astron. **51**, 1333 (2021).

[114] Z. Arzoumanian *et al.* (NANOGRAV Collaboration), Astrophys. J. **859**, 47 (2018).

[115] G. Agazie *et al.* (NANOGrav Collaboration), Astrophys. J. Lett. **951**, L8 (2023).

[116] R. N. Manchester, G. Hobbs, M. Bailes, W. A. Coles, W. van Straten, M. J. Keith, R. M. Shannon, N. D. R. Bhat, A. Brown, S. G. Burke-Spolaor *et al.*, Publ. Astron. Soc. Aust. **30**, 17 (2013).

[117] G. Hobbs, A. Archibald, Z. Arzoumanian, D. Backer, M. Bailes, N. D. R. Bhat, M. Burgay, S. Burke-Spolaor, D. Champion, I. Cognard *et al.*, Classical Quantum Gravity **27**, 084013 (2010).

[118] A. Weltman, P. Bull, S. Camera, K. Kelley, H. Padmanabhan, J. Pritchard, A. Raccanelli, S. Riemer-Sørensen, L. Shao, S. Andrianomena *et al.*, Publ. Astron. Soc. Aust. **37**, e002 (2020).

[119] K. Schmitz, J. High Energy Phys. 01 (2021) 097.

[120] A. Aboubrahim, M. M. Altakach, M. Klasen, P. Nath, and Z. Y. Wang, J. High Energy Phys. 03 (2023) 182.

[121] N. Aghanim *et al.* (Planck Collaboration), Astron. Astrophys. **641**, A6 (2020); **652**, C4(E) (2021).

[122] X. Wang, F. P. Huang, and X. Zhang, J. Cosmol. Astropart. Phys. 05 (2020) 045.

[123] X. Wang, F. P. Huang, and Y. Li, Phys. Rev. D **105**, 103513 (2022).

[124] M. Laine, Phys. Rev. D **49**, 3847 (1994).

[125] A. Ekstedt, P. Schicho, and T. V. I. Tenkanen, Comput. Phys. Commun. **288**, 108725 (2023).

[126] T. Matsubara, Prog. Theor. Phys. **14**, 351 (1955).

[127] M. E. Carrington, Phys. Rev. D **45**, 2933 (1992).

[128] D. Comelli and J. R. Espinosa, Phys. Rev. D **55**, 6253 (1997).

[129] A. Katz and M. Perelstein, J. High Energy Phys. 07 (2014) 108.

[130] S. R. Coleman and E. J. Weinberg, Phys. Rev. D **7**, 1888 (1973).

[131] G. W. Anderson and L. J. Hall, Phys. Rev. D **45**, 2685 (1992).

[132] M. Dine, R. G. Leigh, P. Y. Huet, A. D. Linde, and D. A. Linde, Phys. Rev. D **46**, 550 (1992).

[133] O. Matsedonskyi and G. Servant, J. High Energy Phys. 09 (2020) 012.

[134] A. Aboubrahim, T. Ibrahim, M. Klasen, and P. Nath, Eur. Phys. J. C **81**, 680 (2021).

[135] M. Hindmarsh and O. Philipsen, Phys. Rev. D **71**, 087302 (2005).

[136] L. Husdal, Galaxies **4**, 78 (2016).

[137] E. W. Kolb and M. S. Turner, Front. Phys. **69**, 1 (1990).

[138] D. Pappadopulo, J. T. Ruderman, and G. Trevisan, Phys. Rev. D **94**, 035005 (2016).